Supporting Information:

Electrocatalytic Ammonia Oxidation Mediated by a Polypyridyl Iron Catalyst

Michael D. Zott,[‡] Pablo Garrido-Barros,[‡] and Jonas C. Peters*

Division of Chemistry and Chemical Engineering, California Institute of Technology (Caltech), Pasadena, California 91125, United States

*Corresponding author email: jpeters@caltech.edu

Contents:

S1. General Procedures

General Considerations: All manipulations were carried out using standard Schlenk or glovebox techniques under an N_2 or Ar atmosphere. Unless otherwise noted, solvents were deoxygenated and dried by thoroughly sparging with N_2 gas followed by passage through an activated alumina column in the solvent purification system by SG Water, USA LLC. For electrochemical measurements under an Ar atmosphere, solvents were further degassed and then left under Ar. All solvents were stored over activated 4 Å molecular sieves prior to use. Anhydrous ammonia gas was dried by passage through a calcium oxide drying tube. All reagents were purchased from commercial vendors and used without further purification unless otherwise stated. Tris(2-pyridylmethyl)amine (TPA)[1] and tris(2-pyridylmethylamine) iron(II) triflate bis acetonitrile[2] were synthesized according to literature procedures. $^{15}NH_4OTf$ was prepared from $^{15}NH_4Cl$ (Cambridge Isotope Laboratories) by anion exchange with silver triflate followed by repeated recrystallization from acetonitrile. ^{1}H NMR chemical shifts are reported in ppm relative to tetramethylsilane, using residual solvent resonances as internal standards.

Electrochemistry: Cyclic Voltammetry (CV), Linear Sweep Voltammetry (LSV), Differential Pulse Voltammetry (DPV) and Controlled Potential Coulometry (CPC) experiments were carried out with a Biologic VSP-300 potentiostat using a one-compartment three-electrode cell. For CV, LSV and DPV, a Boron Doped Diamond (BDD) disk electrode (3 mm diameter) was used as the working electrode, Pt wire as the counter electrode, and a Ag/AgOTf reference electrode was employed using an acetonitrile solution containing 5 mM AgOTf and 0.1 M $TBAPF_6$. For CPE, the same reference electrode was used, but a BDD plate (geometric area: 1 cm^2) and a Pt mesh were used respectively as working and counter electrode. All redox potentials in the present work are reported versus the Fc/Fc^+ couple, measured before each experiment to be +0.115 V versus our Ag/AgOTf reference electrode.

CVs and LSVs were collected at 100 $mV \cdot s^{-1}$ unless specified otherwise. DPVs were obtained with the following parameters: amplitude = 50 mV, step height = 4 mV, pulse width = 0.05 s, pulse period = 0.5 s and sampling width = 0.0167 s. $E_{1/2}$ values for the reversible waves were obtained from the half potential between the oxidative and reductive peaks. All measurements were performed applying IR compensation, compensating 85% of the resistance measured at one high frequency value (100 kHz).

Gas Chromatography: Gas chromatography was performed in the Environmental Analysis Center using HP 5890 Series II instruments. Gas quantification was performed using a molecular sieve column attached to a thermal conductivity detector. Argon was the carrier gas. Standard curves were generated by direct injection of hydrogen or nitrogen gas. Quantification of background nitrogen was determined using the background oxygen signal. Isotopic measurements were performed with a separate HP 5890 Series II equipped with a GasPro column using helium as the carrier gas.

NMR: NMR spectroscopy was performed using a Varian 400 MHz NMR spectrometer equipped with a broadband auto-tune probe. ^{1}H NMR chemical shifts are reported in ppm relative to tetramethylsilane, using residual solvent resonances as internal standards.

Mössbauer: Spectra were recorded on a spectrometer from SEE Co. operating in the constant acceleration mode in a transmission geometry. Spectra were recorded with the temperature of the sample maintained at 80 K or 100 K. The sample was kept in an SVT-400 Dewar from Janis. The quoted isomer shifts are relative to the centroid of the spectrum of a metallic foil of α-Fe at room temperature. Data analysis was performed using the program WMOSS (www.wmoss.org) and quadrupole doublets were fit to Lorentzian lineshapes.

UV-Vis: Spectra were collected using a Cary 60 instrument with Cary WinUV software.

IR: Spectra were obtained using a Bruker Alpha Platinum ATR spectrometer with OPUS software in a glovebox under an N_2 atmosphere.

X-Ray Crystallography: XRD studies were carried out at the Beckman Institute Crystallography Facility on a Bruker D8 Venture diffractometer (Cu Kα radiation). Structures were solved using direct methods with SHELXS or SHELXT and refined against F^2 on all data by full-matrix least squares with SHELXL.[3] All of the solutions were performed in the Olex2 program.[4] The crystals were mounted on a glass fiber under Paratone N oil.

S2. Catalytic controlled potential coulometry experiments

Procedures for controlled potential coulometry

Preparation of the BDD electrode: A 2 cm^2 boron-doped diamond (BDD) plate electrode (Element Six Technologies, Santa Clara, CA) was connected to standard electrical wire using conductive silver epoxy. The silver epoxy was then covered in Loctite 9460 (Hysol) epoxy to protect the electrical connection from contact with chemical reagents. After covering with epoxy, the total exposed surface geometric area decreased to around 1 cm^2.

BDD has a surface that exists in various states of reduction (H-terminated) and oxidation (O-terminated).[5] In order to remove attached nitrogen and iron generated during controlled potential coulometry experiments and to ensure a reliable electrode surface prior to CPC measurements, the BDD plate electrode was oxidatively treated prior to use. First, the electrode was soaked in concentrated nitric acid for 5 minutes. Then, a potential of 3.0 V vs Ag/AgCl was applied to the BDD electrode in a 0.5 M H_2SO_4 solution for 10 minutes. The electrode was then thoroughly rinsed with water prior to use.

Preparation of the platinum counter electrode: In order to ensure a highly active Pt surface for HER prior to CPC experiments, the Pt mesh counter electrode was soaked in concentrated hydrochloric acid for at least 5 minutes prior to usage.

Preparation of the custom Ag/AgOTf reference electrode: To ensure reliable potential measurements, the custom Ag/AgOTf reference electrode was prepared prior to each CPC experiment and then a CV of ferrocene was measured. In a glass tube fitted with a Vycor porous glass frit attached by Teflon heatshrink tubing, an acetonitrile solution containing 5 mM AgOTf and 0.1 M $TBAPF_6$ was added. A silver wire was placed inside and the electrode was sealed.

Preparation of ammonia solutions. For experiments with natural abundance ammonia, saturated 2 M solutions[6] in acetonitrile were prepared by bubbling anhydrous ammonia through acetonitrile in a Schlenk tube under an argon atmosphere. For experiments with labeled $^{15}NH3$, ammonia was liberated from $^{15}NH_4OTf$ by addition of 1.1 equivalents of 1,8-Diazabicyclo[5.4.0]undec-7-ene (DBU) to ammonium triflate dissolved in acetonitrile in a Schlenk tube inside of an argon glovebox. This solution was then vacuum transferred to a separate clean Schlenk tube.

CPC: Inside an argon glovebox, a gas-tight electrochemical cell equipped with a 24/40 cap containing three tungsten rods for electrical contacts and a 14/20 joint carefully sealed with a Suba-Seal septum was prepared. A BDD plate electrode (A = 1 cm^2), high surface area platinum mesh electrode, and custom Ag/AgOTf reference electrode were connected to the 24/40 cap. All chemical reagents were then rapidly added to the cell to prevent evaporation of ammonia and then the cell was sealed with the 24/40 cap. Prior to each CPC, a ZIR and CV were taken. Then, manual IR compensation using 85% of the uncompensated resistance determined by the ZIR measurement was applied and the CPC was started. At the end of the CPC experiment, another CV was taken to assess any difference in current pre- and post-CPC. The cell was then removed from the glovebox for analysis by gas chromatography. For headspace analysis, 100 μL of the headspace was injected

into a GC-TCD for quantification using a lockable Hamilton syringe with a 26S gauge needle. For GC-MS, only 50 µL of the headspace was injected.

For each experiment, a 10 mL solution containing 0.5 mM $[(TPA)Fe(MeCN)_2]OTf_2$ (3.6 mg), 65 mM NH_3 (0.33 mL of 2.0 M solution), and 50 mM NH_4OTf (83.6 mg) was prepared in acetonitrile. For experiments with 2.5 µmol [Fe], 5.0 mL of this solution was added to the electrochemical cell. Otherwise, the entire 10 mL portion was added.

Table S1: Results of catalytic CPC experiments.

Entry	Fe Source	Eq. N_2	µmol [Fe]	Charge (C)	FE N_2 (%)	FE H_2 (%)
1	(TPA)Fe	18.1	2.5	37.1	70	62
2	(TPA)Fe	16.4	2.5	29.7	79	66
3	(TPA)Fe	9.4	5	30.8	87	70
4	(TPA)Fe	10.6	5	40.6	75	72
5*	(TPA)Fe	9.6	5	29.8	93	74
6*	(TPA)Fe	7.5	5	28.6	75	69

* Experiment performed with $^{15}NH_3$ and $^{15}NH_4OTf$

Table S2: Results of control CPC experiments. For control experiments, the electrochemical cell was filled with the entire 10 mL acetonitrile solution of 65 mM NH_3 and 50 mM NH_4OTf.

Entry	Fe Source	Eq. N_2	µmol [Fe]	Charge (C)
1	None	0.5†	0	1.05
2	$FeOTf_2$	1.0	5	1.89

† For the NH_3 only control experiment, one equivalent is set equal to the number of moles of iron in the corresponding catalytic experiment i.e. 5 mmol.

S3. Chronoamperograms for catalytic and control experiments

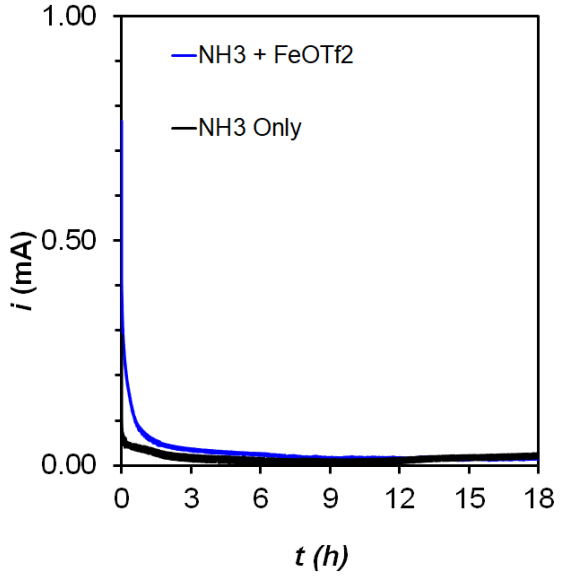

Figure S1: Chronoamperograms corresponding to 18 h CPC background measurements with 50 mM NH_4OTf supporting electrolyte with (black) only 65 mM NH_3 and (blue) 65 mM NH_3 with 0.5 mM $FeOTf_2$.

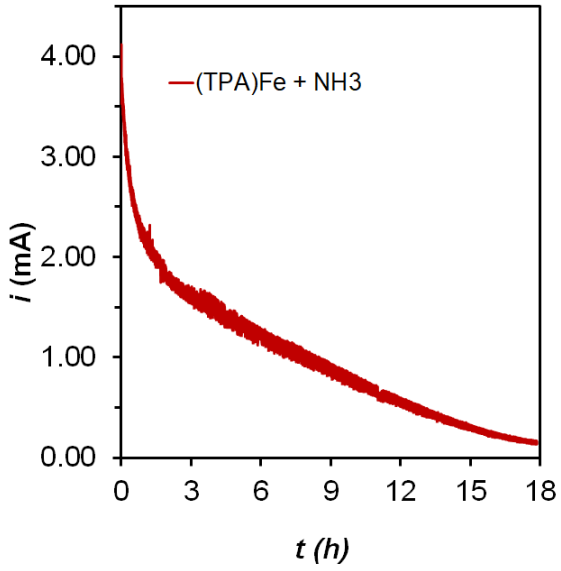

Figure S2: Chronoamperogram corresponding to 18 h CPC catalytic experiment with 0.5 mM $[(TPA)Fe(MeCN)_2]OTf_2$, 65 mM NH_3, and 50 mM NH_4OTf supporting electrolyte.

S4. Cyclic voltammograms with BDD plate/disk electrode pre- and post-CPC

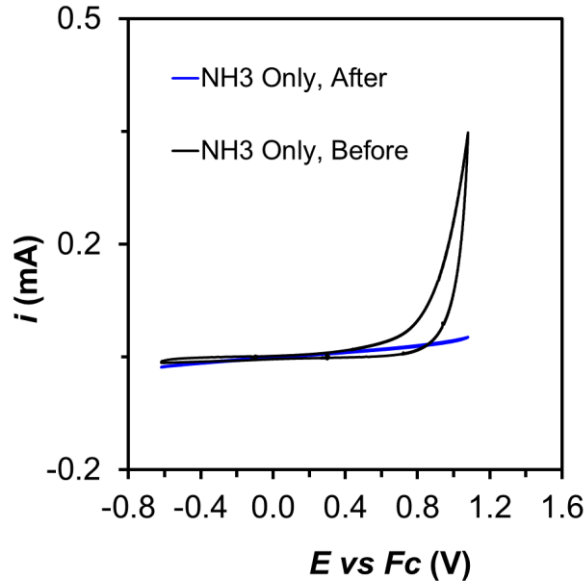

Figure S3: CVs of 65 mM NH_3 solution with 50 mM NH_4OTf supporting electrolyte before (black trace) and after (blue trace) 18 hours of controlled potential coulometry at 1.1 V vs Fc/Fc^+. The decrease in current is due to passivation of the electrode surface.

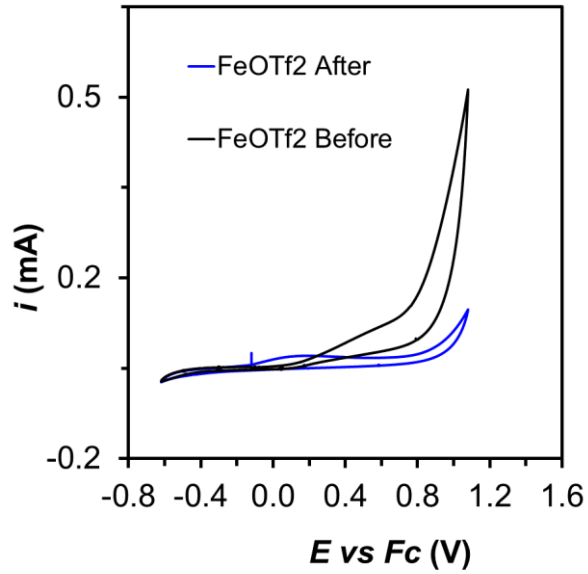

Figure S4: CVs of 0.5 mM $FeOTf_2$ solution with 65 mM NH_3 and 50 mM NH_4OTf supporting electrolyte before (black trace) and after (blue trace) 18 hours of controlled potential coulometry at 1.1 V vs Fc/Fc^+. The decrease in current is due to passivation of the electrode surface.

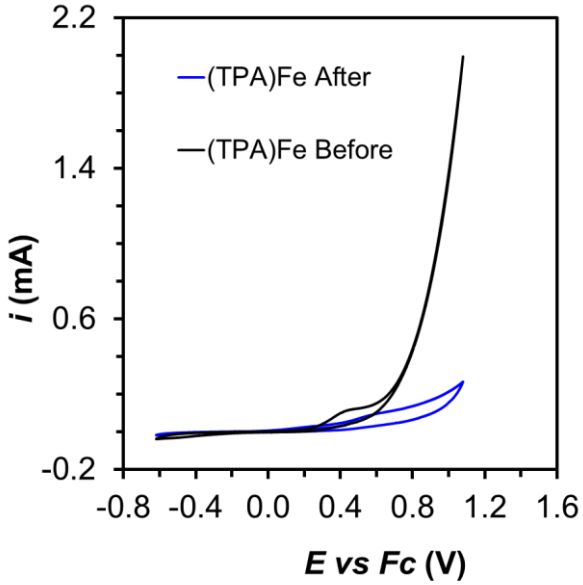

Figure S5: CVs of 0.5 mM [(TPA)Fe(MeCN)$_2$]OTf$_2$ solution with 65 mM NH_3 and 50 mM NH_4OTf supporting electrolyte before (black trace) and after (blue trace) 18 hours of controlled potential coulometry at 1.1 V vs Fc/Fc^+. The decrease in current is due to passivation of the electrode surface.

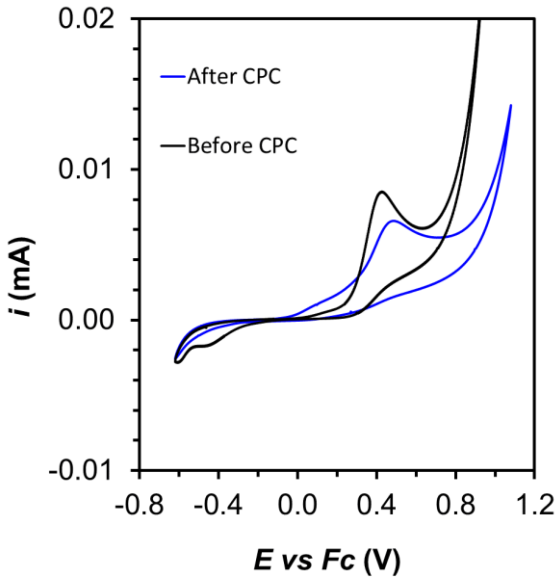

Figure S6: Cyclic voltammograms of 0.5 mM [(TPA)Fe(MeCN)$_2$]OTf$_2$ solution with BDD disk electrode before and after 18 h CPC experiment.

S5. UV-Vis spectra of catalytic mixture pre- and post-CPC

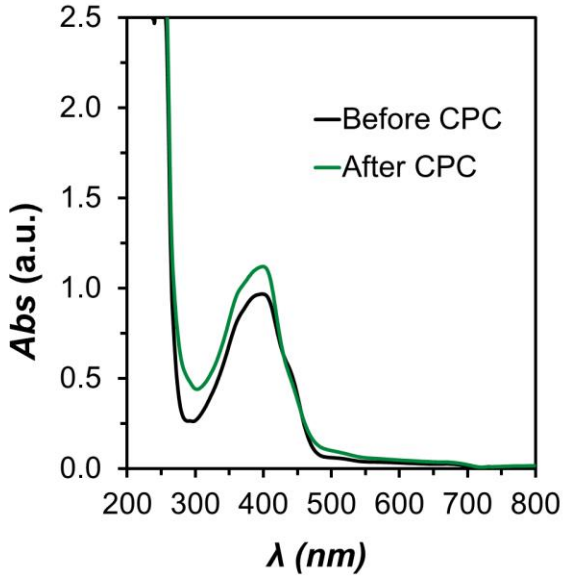

Figure S7: UV-Vis spectrum of 0.2 mM [(TPA)Fe(MeCN)$_2$]OTf$_2$ solution diluted from 0.5 mM [(TPA)Fe(MeCN)$_2$]OTf$_2$ solution before and after 18 h CPC experiment.

Figures S6 and S7 provide evidence that after 18 h of CPC, the [(TPA)Fe(MeCN)$_2$]OTf$_2$ solution from catalytic experiments still contains active [(TPA)Fe(L)$_2$]$^{2+}$. Exact quantification of catalyst present before and after catalysis is difficult due to the speciation of [(TPA)Fe(L)$_2$]OTf$_2$ with varying ammonia concentrations. As the ammonia concentration decreases, the absorbance at 400 nm increases in this concentration range, further complicating analysis.

S6. GC-MS and GC-TCD traces

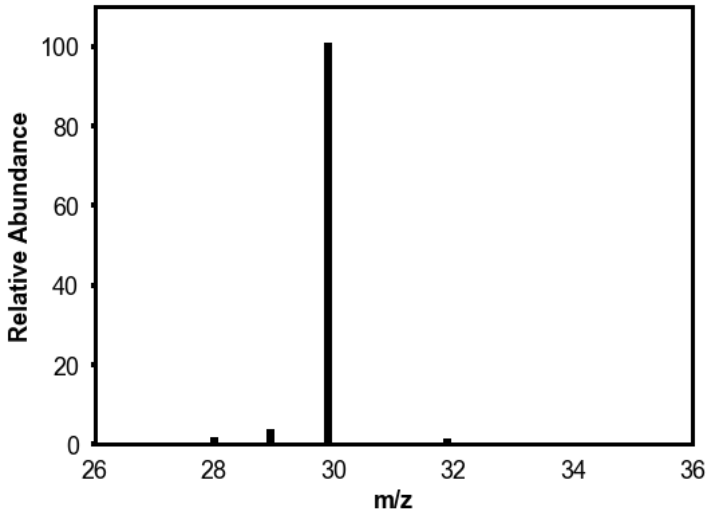

Figure S8: GC-MS data for representative catalytic experiment with 5 µmol $[(TPA)Fe(MeCN)_2]OTf_2$ performed with $^{15}NH_3$ and $^{15}NH_4OTf$.

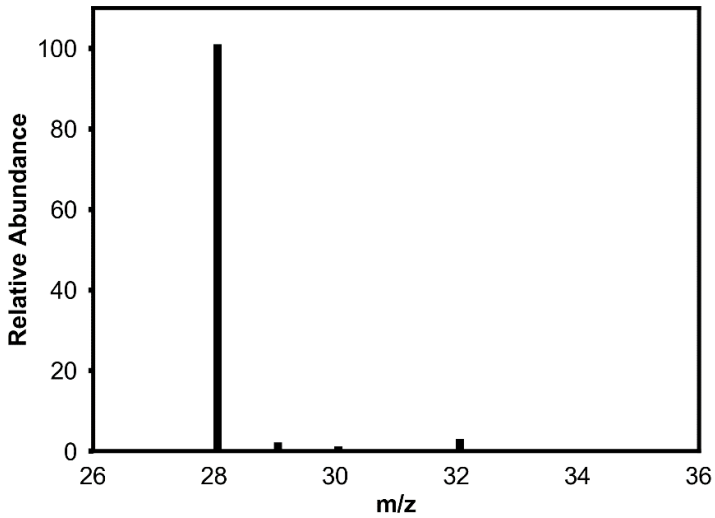

Figure S9: GC-MS data for representative catalytic experiment with 5 µmol $[(TPA)Fe(MeCN)_2]OTf_2$ performed with natural abundance NH_3 and NH_4OTf.

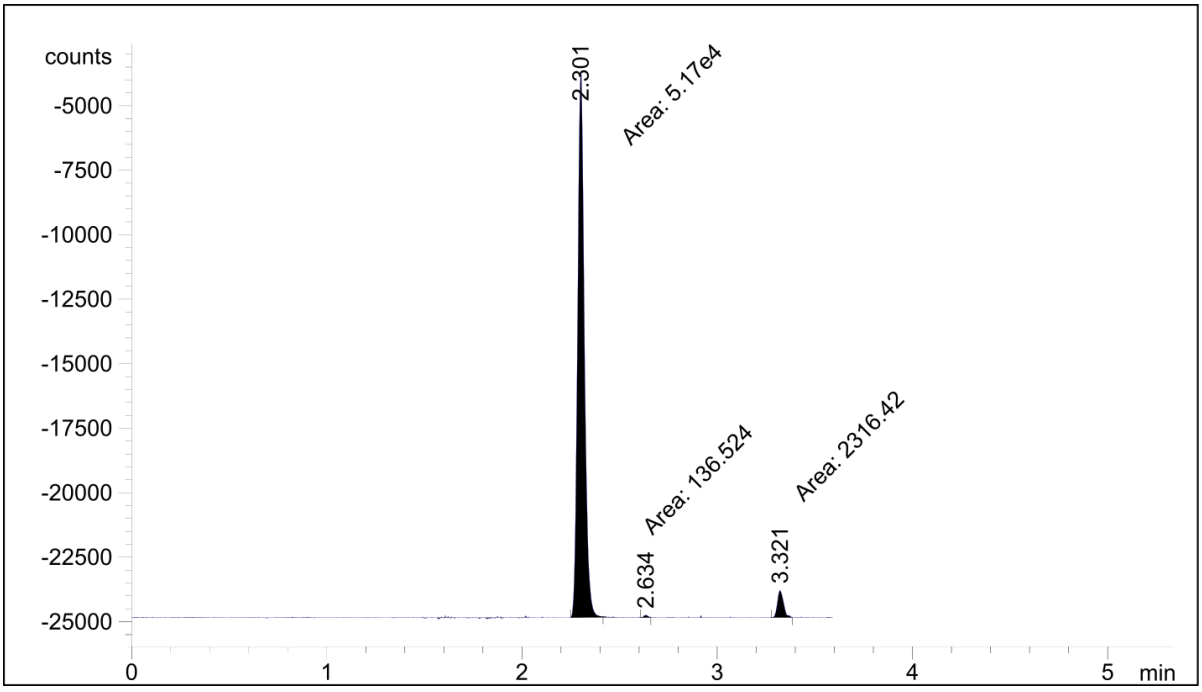

Figure S10: Representative GC-TCD trace showing H_2 (RT = 2.3 min), O_2 (RT = 2.6 min), and N_2 (RT = 3.3 min).

S7. Standard curves for quantification of N_2 and H_2

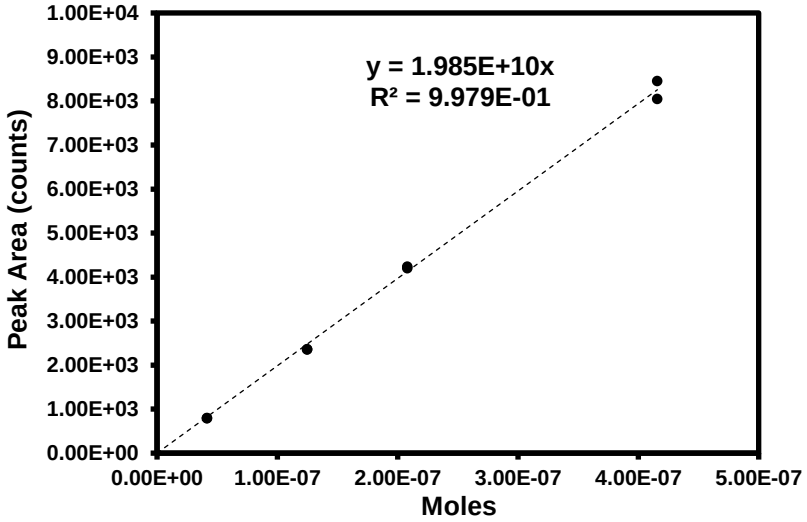

Figure S11: Standard curve for quantification of N_2 generated by direct injection of N_2 gas from a Suba-Seal rubber septum capped Schlenk tube.

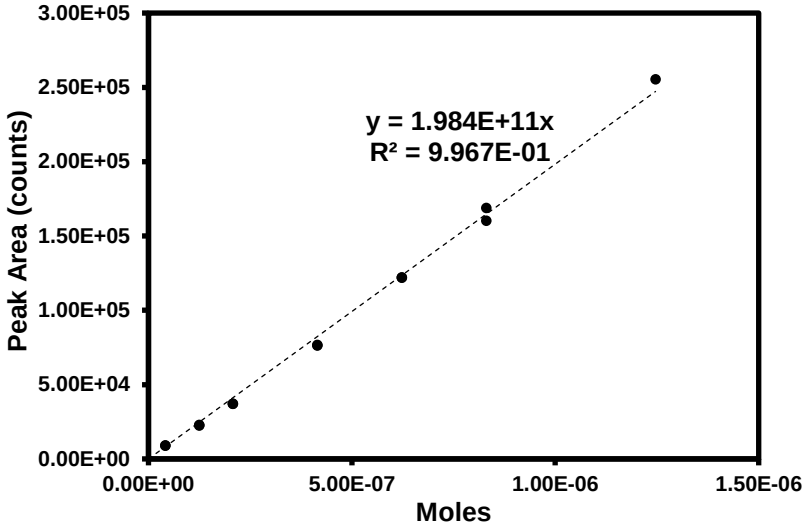

Figure S12: Standard curve for quantification of H_2 generated by direct injection of H_2 gas from a Suba-Seal rubber septum capped Schlenk tube.

S8. CV cycling experiments and rinse tests

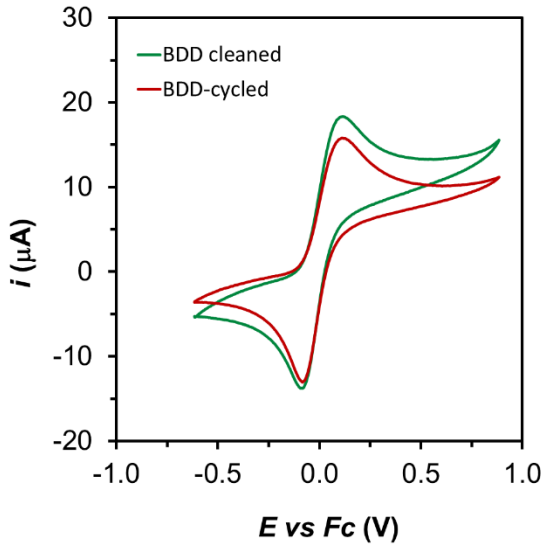

Figure S13: Cyclic voltammograms of acetonitrile solution containing 1 mM Fc using the rinsed BDD disk electrode before and after 50 CV cycles in acetonitrile solution with 2.5 mM $[(TPA)Fe(MeCN)_2]OTf_2$, 0.05 M NH_3 and 0.05 M NH_4OTf. The scan rate was set to 0.1 $V \cdot s^{-1}$, Pt was used as the counter electrode, with a custom Ag/AgOTf reference electrode.

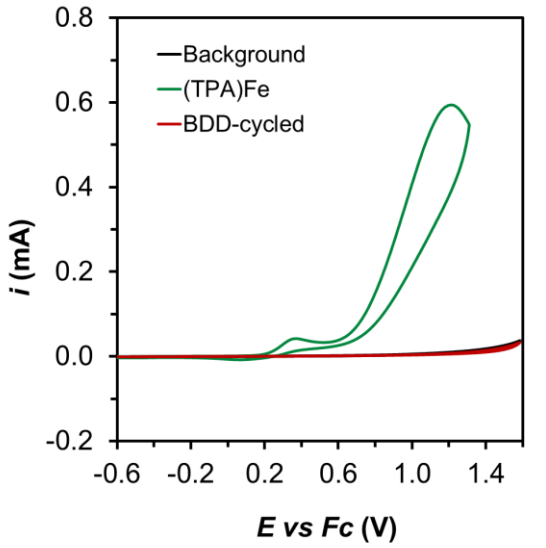

Figure S14: Cyclic voltammograms of acetonitrile solution containing 0.05 M NH_3 and 0.05 M NH_4OTf using a clean BDD electrode (black trace) or the rinsed BDD disk electrode after 50 CV cycles with $[(TPA)Fe(MeCN)_2]OTf_2$ (red trace), showing that no active material was deposited. The green trace depicts the CV of 2.5 mM $[(TPA)Fe(MeCN)_2]OTf_2$ under the same conditions.

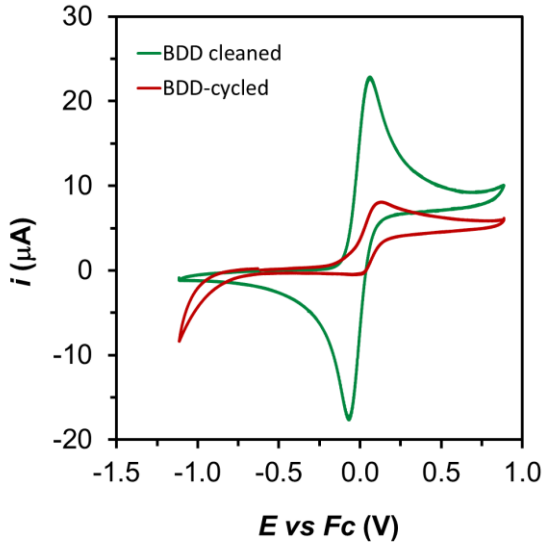

Figure S15: Cyclic voltammograms of acetonitrile solution containing 1 mM Fc using the rinsed BDD disk electrode before and after 50 CV cycles in acetonitrile solution with 2.5 mM $FeOTf_2$, 0.05 M NH_3 and 0.05 M NH_4OTf. The scan rate was set to 0.1 $V \cdot s^{-1}$, Pt was used as the counter electrode, with a custom Ag/AgOTf reference electrode.

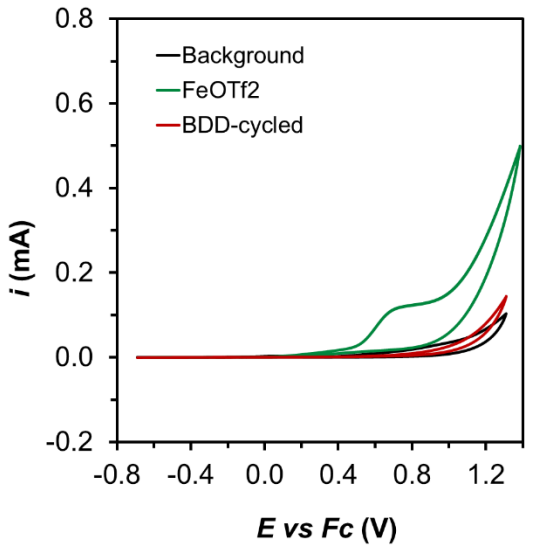

Figure S16: Cyclic voltammograms of acetonitrile solution containing 0.05 M NH_3 and 0.05 M NH_4OTf using a clean BDD electrode (black trace) or the rinsed BDD disk electrode after 50 CV cycles with $FeOTf_2$ (red trace), showing that no active material was deposited. The green trace depicts the CV of a 2.5 mM $FeOTf_2$ under the same conditions.

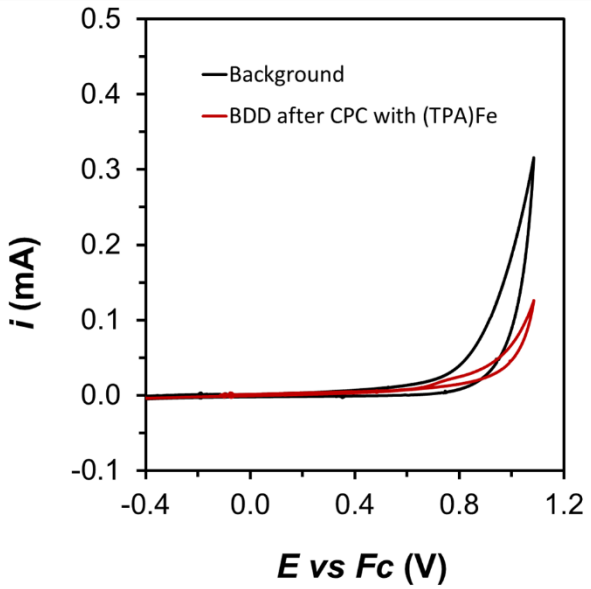

Figure S17: Cyclic voltammograms of acetonitrile solution containing 0.05 M NH_3 and 0.05 M NH_4OTf using a clean BDD electrode (black trace) and the rinsed BDD disk electrode after CPC for 18 hours using 0.5 mM $[(TPA)Fe(MeCN)_2]OTf_2$ as catalyst (red trace). Results show that no active material was deposited, but significant passivation is observed.

S9. XPS spectra of BDD plate electrode

Procedures for XPS: For XPS measurements, the BDD plate electrode was dipped into fresh acetonitrile twice to remove any soluble components. Then, the electrode was left in a 60^{o} C vacuum oven overnight to decrease off-gassing in the sample chamber. XPS measurements are corrected for surface charging by setting the binding energy of the carbon 1s peak to be 285 eV. This correction was always less than 1 eV. A full scan from 0-1000 eV was acquired, and then scans at the binding energies typical for carbon (274-294 eV), boron (176-196 eV), nitrogen (389-409 eV), oxygen (522-542 eV), and iron (690-730 eV) were measured.

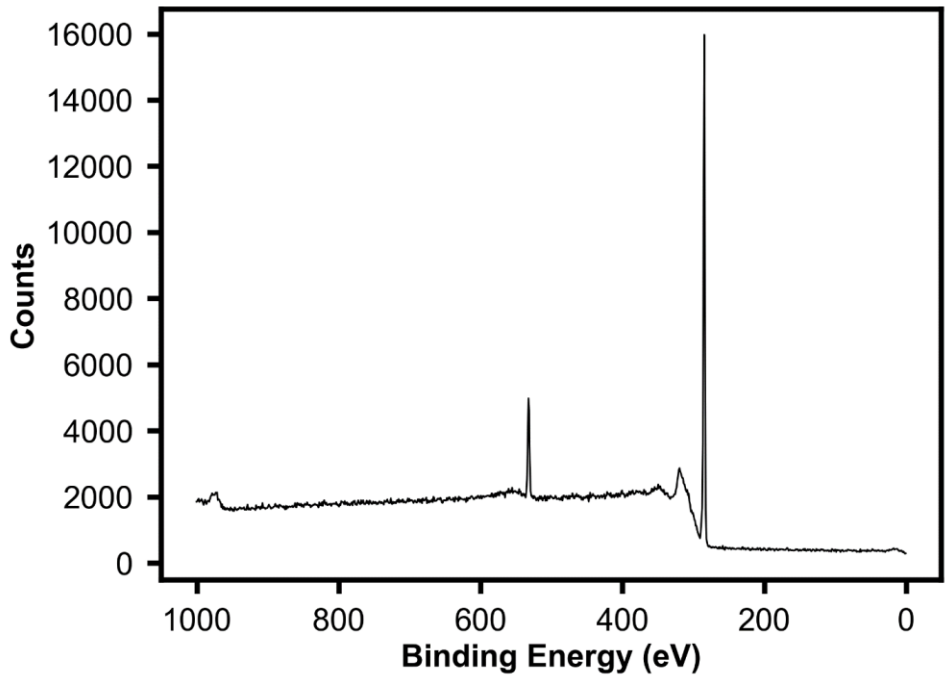

Figure S18: XPS spectrum of BDD plate electrode before AO conditions. Binding energy is corrected for surface charging by setting C1s to be 285 eV.

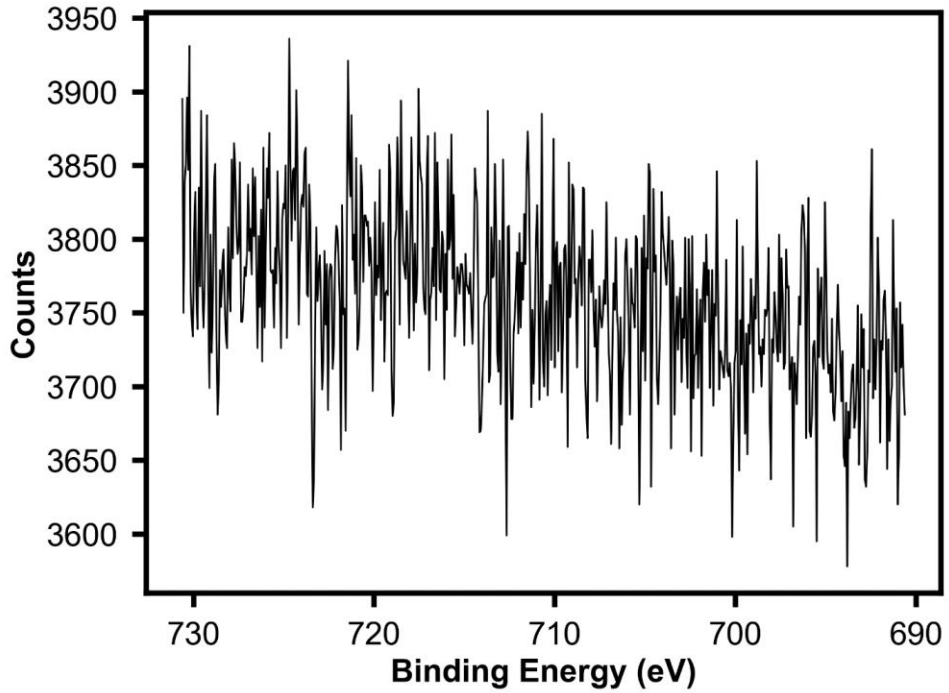

Figure S19: XPS spectrum of BDD plate electrode before AO conditions centered on the region characteristic for Fe 2p. Binding energy is corrected for surface charging by setting C1s to be 285 eV.

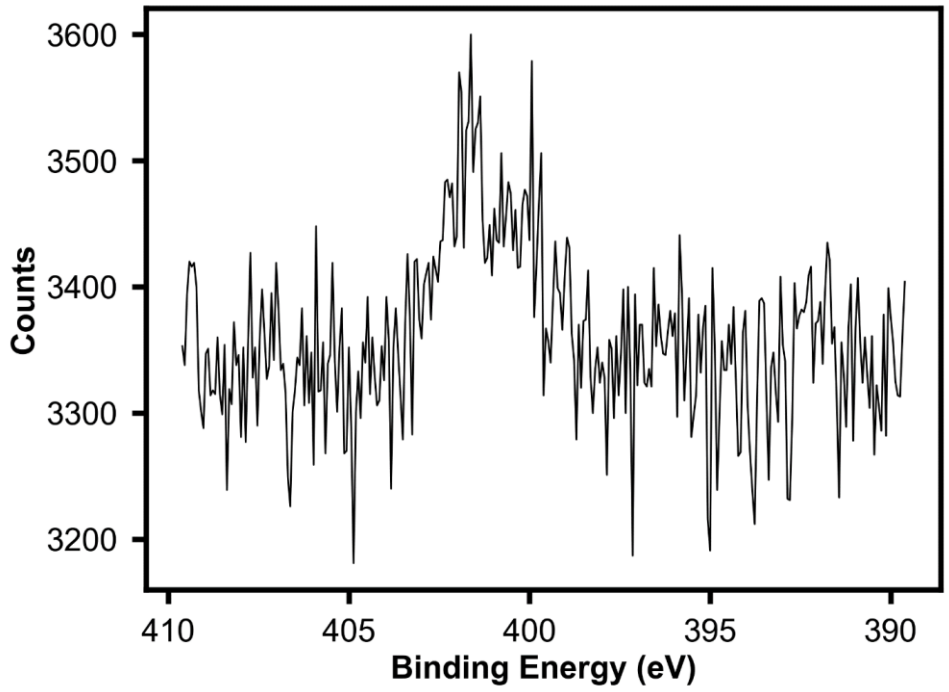

Figure S20: XPS spectrum of BDD plate electrode before AO conditions centered on the region characteristic for N 1s. Binding energy is corrected for surface charging by setting C1s to be 285 eV.

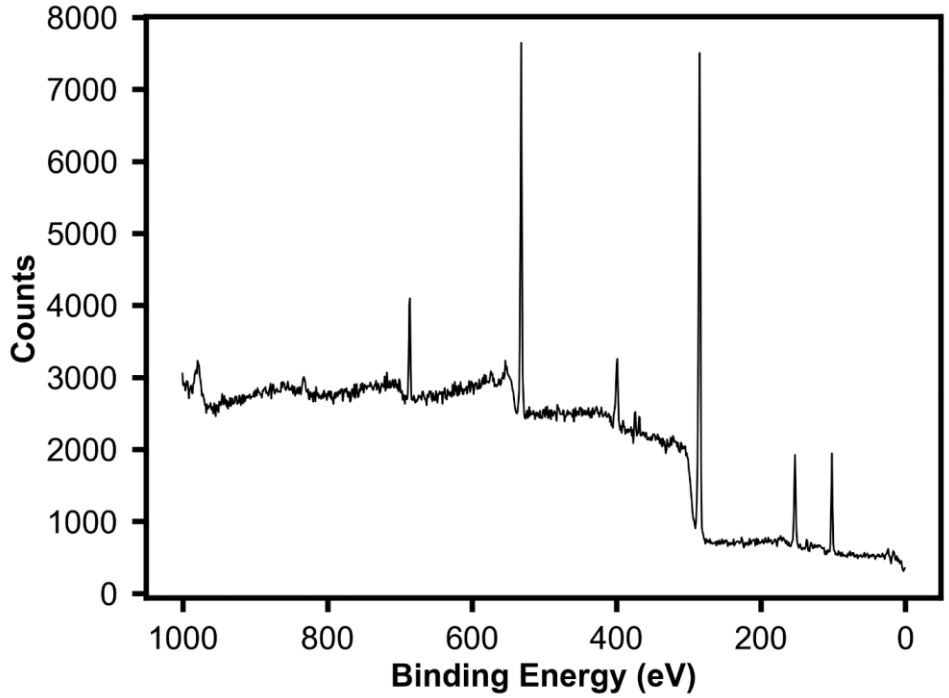

Figure S21: XPS spectrum of BDD plate electrode after 18 h CPC with 65 mM NH_3 solution. Binding energy is corrected for surface charging by setting C1s to be 285 eV.

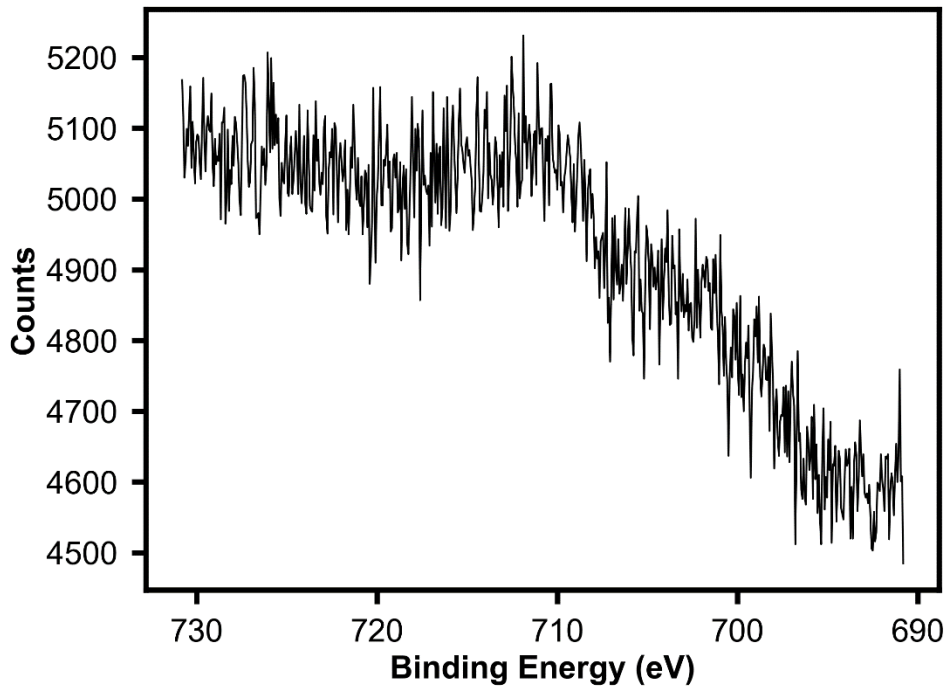

Figure S22: XPS spectrum of BDD plate electrode after 18 h CPC with 65 mM NH_3 solution centered on the region characteristic for Fe 2p. Binding energy is corrected for surface charging by setting C1s to be 285 eV.

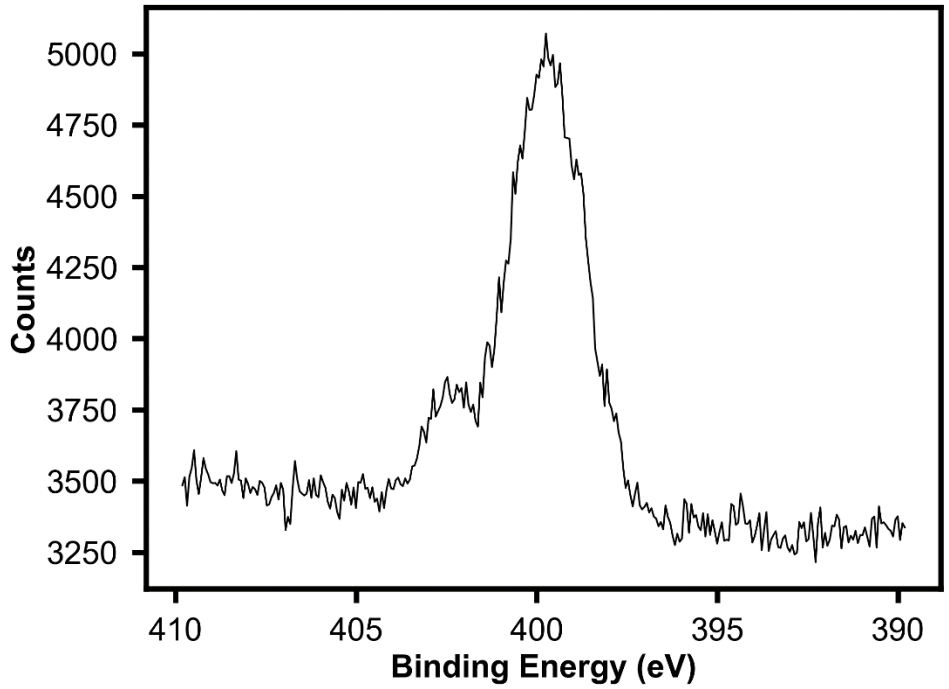

Figure S23: XPS spectrum of BDD plate electrode after 18 h CPC with 65 mM NH_3 solution centered on the region characteristic for N 1s. Binding energy is corrected for surface charging by setting C1s to be 285 eV.

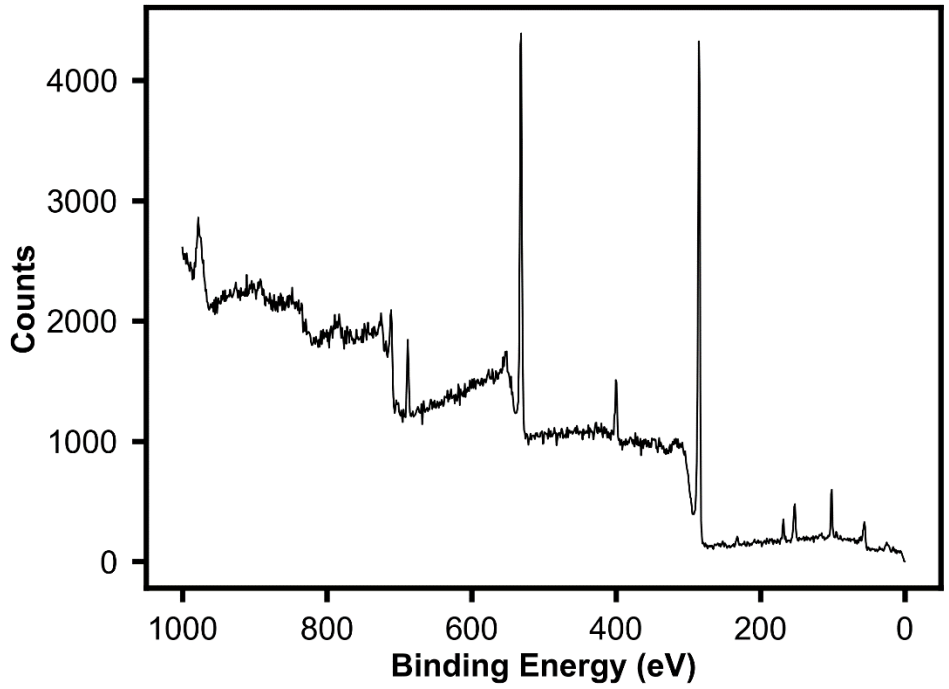

Figure S24: XPS spectrum of BDD plate electrode after 18 h CPC with 0.5 mM $[(TPA)Fe(MeCN)_2]OTf_2$ and 65 mM NH_3 solution. Binding energy is corrected for surface charging by setting C1s to be 285 eV.

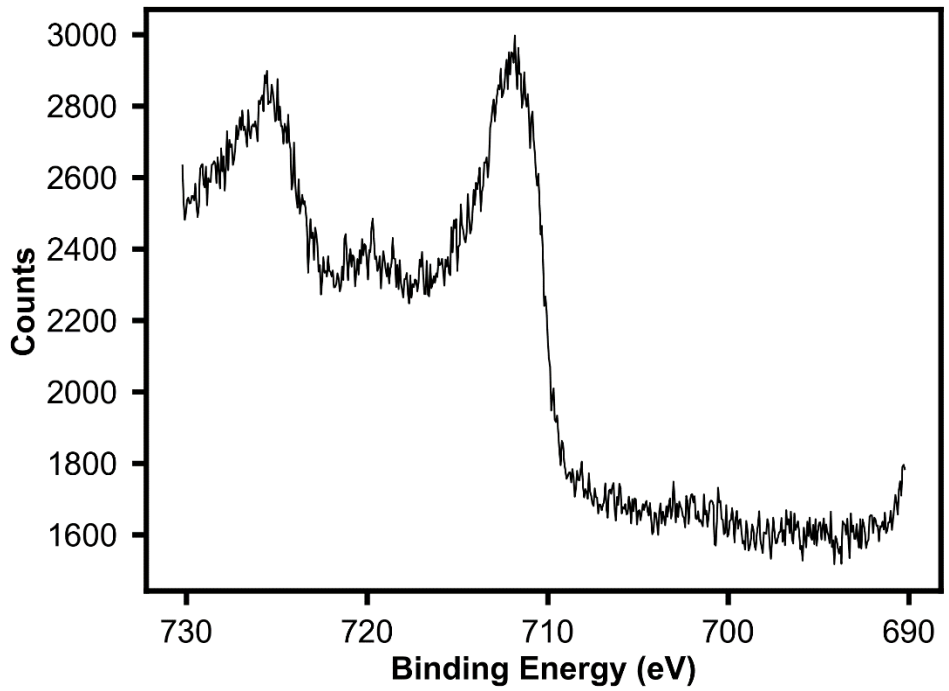

Figure S25: XPS spectrum of BDD plate electrode after 18 h CPC with 0.5 mM [(TPA)Fe(MeCN)$_2$]OTf$_2$ and 65 mM NH_3 solution centered on the region characteristic for Fe 2p. Binding energy is corrected for surface charging by setting C1s to be 285 eV.

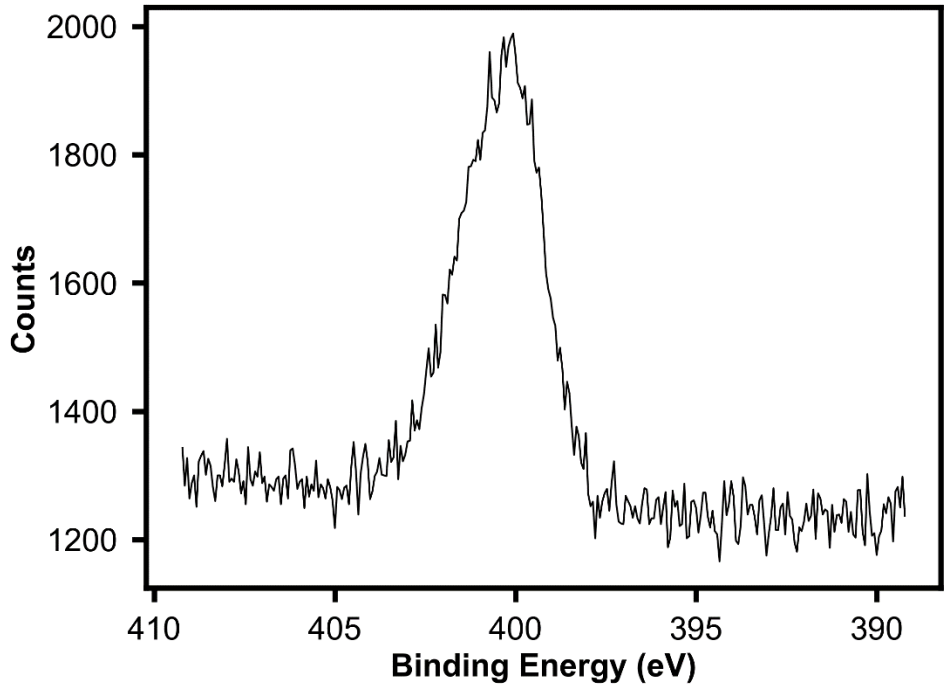

Figure S26: XPS spectrum of BDD plate electrode after 18 h CPC with 0.5 mM [(TPA)Fe(MeCN)$_2$]OTf$_2$ and 65 mM NH_3 solution centered on the region characteristic for N 1s. Binding energy is corrected for surface charging by setting C1s to be 285 eV.

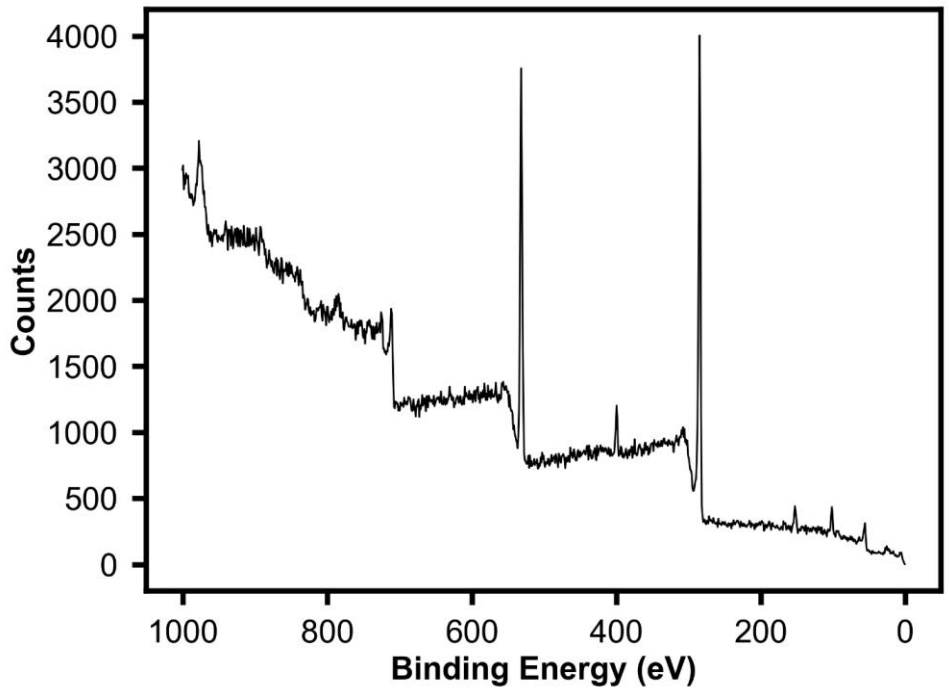

Figure S27: XPS spectrum of BDD plate electrode after 18 h CPC with 0.5 mM $FeOTf_2$ and 65 mM NH_3 solution. Binding energy is corrected for surface charging by setting C1s to be 285 eV.

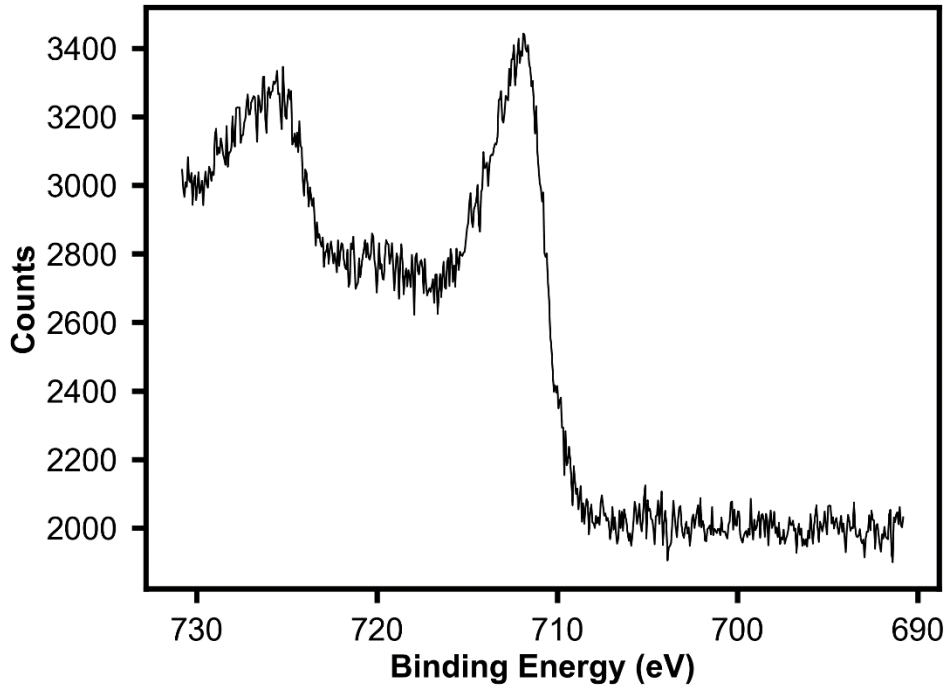

Figure S28: XPS spectrum of BDD plate electrode after 18 h CPC with 0.5 mM $FeOTf_2$ and 65 mM NH_3 solution centered on the region characteristic for Fe 2p. Binding energy is corrected for surface charging by setting C1s to be 285 eV.

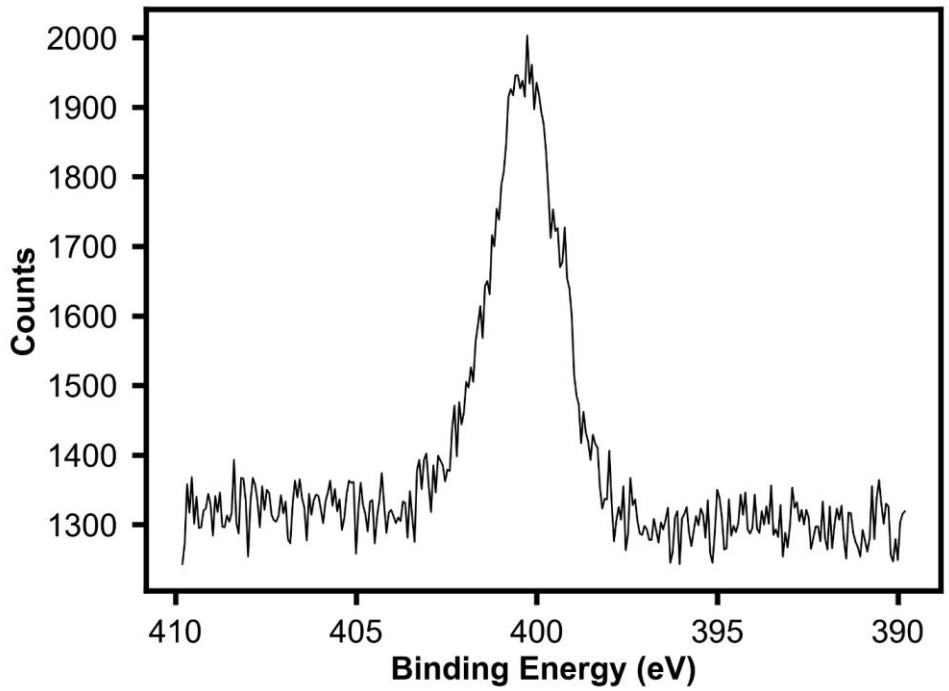

Figure S29: XPS spectrum of BDD plate electrode after 18 h CPC with 0.5 mM $FeOTf_2$ and 65 mM NH_3 solution centered on the region characteristic for N 1s. Binding energy is corrected for surface charging by setting C1s to be 285 eV.

S10. Synthesis and solid-state structure of $[(TPA)Fe(NH_3)_2]OTf_2$

The title compound was prepared by slow diffusion of ammonia gas from a saturated ammonia-THF solution into an acetonitrile free solution of $(TPA)FeOTf_2$ in THF at room temperature. Over the course of 12-24 hours, the clear yellow solution gradually turned orange and orange needles precipitated. These orange needles were confirmed by SC-XRD to be $[(TPA)Fe(NH_3)_2]OTf_2$. Upon cooling the needles to 100 K under the cold stream, they changed color from orange to red, evidence of spin-crossover behavior. The color change was reversible.

$[(TPA)Fe(NH_3)_2]OTf_2$ crystallizes in the space group P $2_1/n$ with four independent cations in the asymmetric unit. At 100 K, two of the iron sites are low spin based on their bond distances (and corresponding solid-state Mössbauer analysis) and the other two sites are high spin. The cations in the crystal structure suffer from disorder at only one of the four iron sites. Unsurprisingly, the triflates are also disordered. Hydrogen atoms were not refined but were placed using a riding model.

To model the disorder at the one disordered iron site, SADI, SIMU, and RIGU restraints were used to model a separate iron unit with head-to-tail like disorder. Positional and rotational disorder of the triflate anions was also modeled with the help of SADI, SIMU, and RIGU restraints. Remaining unmodeled electron density is primarily located near the triflate anions and THF solvent molecules.

Further details are provided in the CIF file that has been electronically uploaded as additional Supporting Information.

Table S3: Crystal data and structure refinement for $[(TPA)Fe(NH_3)_2]OTf_2$.

Temperature/K	99.99
Crystal system	monoclinic
Space group	$P2_1/n$
a/Å	31.690(8)
b/Å	12.063(5)
c/Å	34.405(5)
α/°	90
β/°	109.475(13)
γ/°	90
Volume/Å^3	12399(6)
Z	16
ρ_{calc}g/cm^3	1.573
μ/mm^{-1}	5.952
F(000)	6033.0
Crystal size/mm^3	0.287 × 0.281 × 0.144
Radiation	CuKα (λ = 1.54178)
2Θ range for data collection/°	4.642 to 159.956
Index ranges	$-40 \leq h \leq 38$, $-14 \leq k \leq 15$, $-42 \leq l \leq 43$
Reflections collected	316748
Independent reflections	26746 [R_{int} = 0.0838, R_{sigma} = 0.0384]
Data/restraints/parameters	26746/2397/1991
Goodness-of-fit on F^2	1.097
Final R indexes [I>=2σ (I)]	R_1 = 0.0739, wR_2 = 0.1587
Final R indexes [all data]	R_1 = 0.0812, wR_2 = 0.1623
Largest diff. peak/hole / e Å^{-3}	1.83/-0.89

S11. UV-vis spectroscopy of $[(TPA)Fe(L)_2]^{2+}$ species

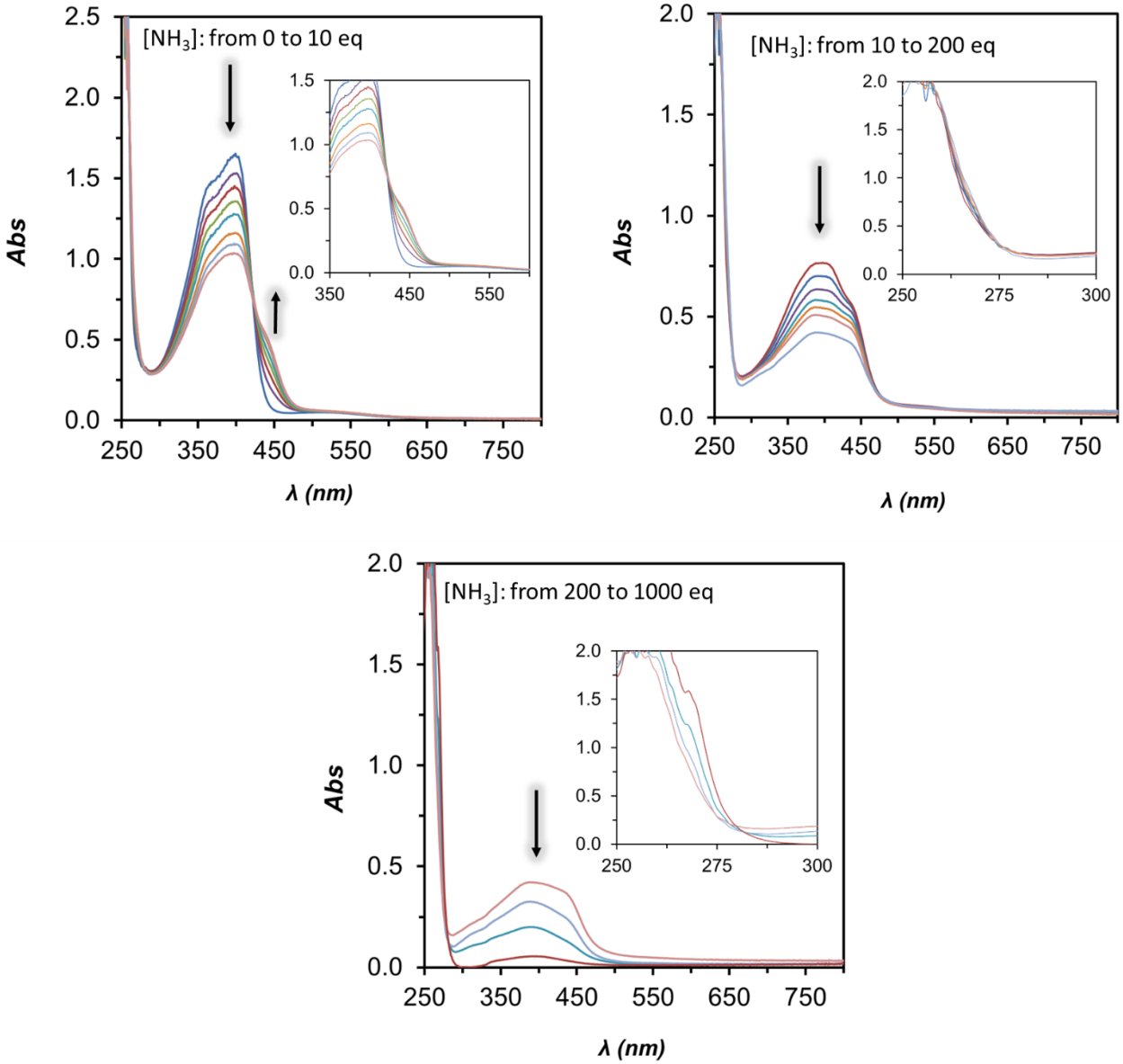

Figure S30: UV-vis spectra of 0.2 mM $[(TPA)Fe(MeCN)_2]OTf_2$ in MeCN with increasing concentrations of NH_3.

S12. ^{1}H NMR spectroscopy of $[(TPA)Fe(L)_2]^{2+}$ species

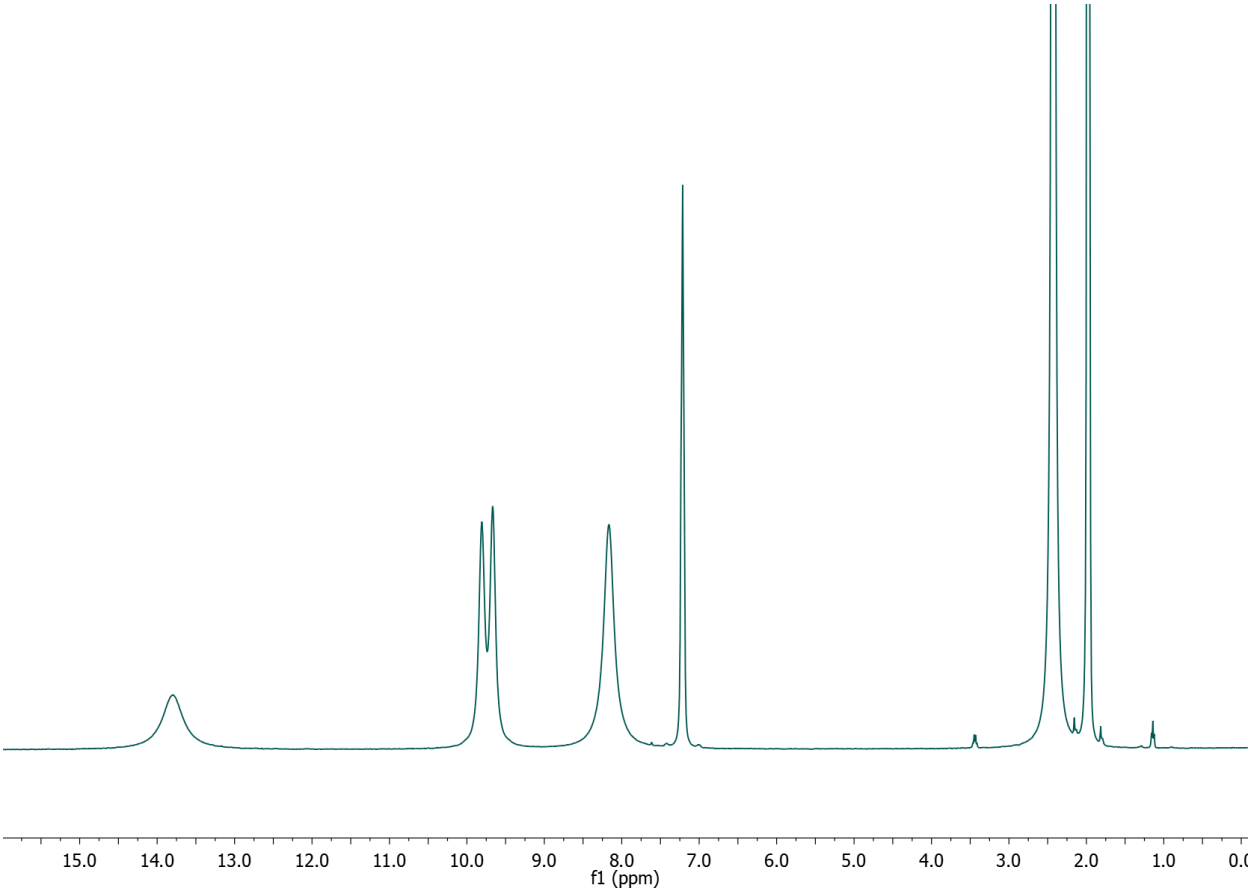

Figure S31: ^{1}H NMR (400 MHz) spectrum of $[(TPA)Fe(MeCN)_2]OTf_2$ in CD_3CN.

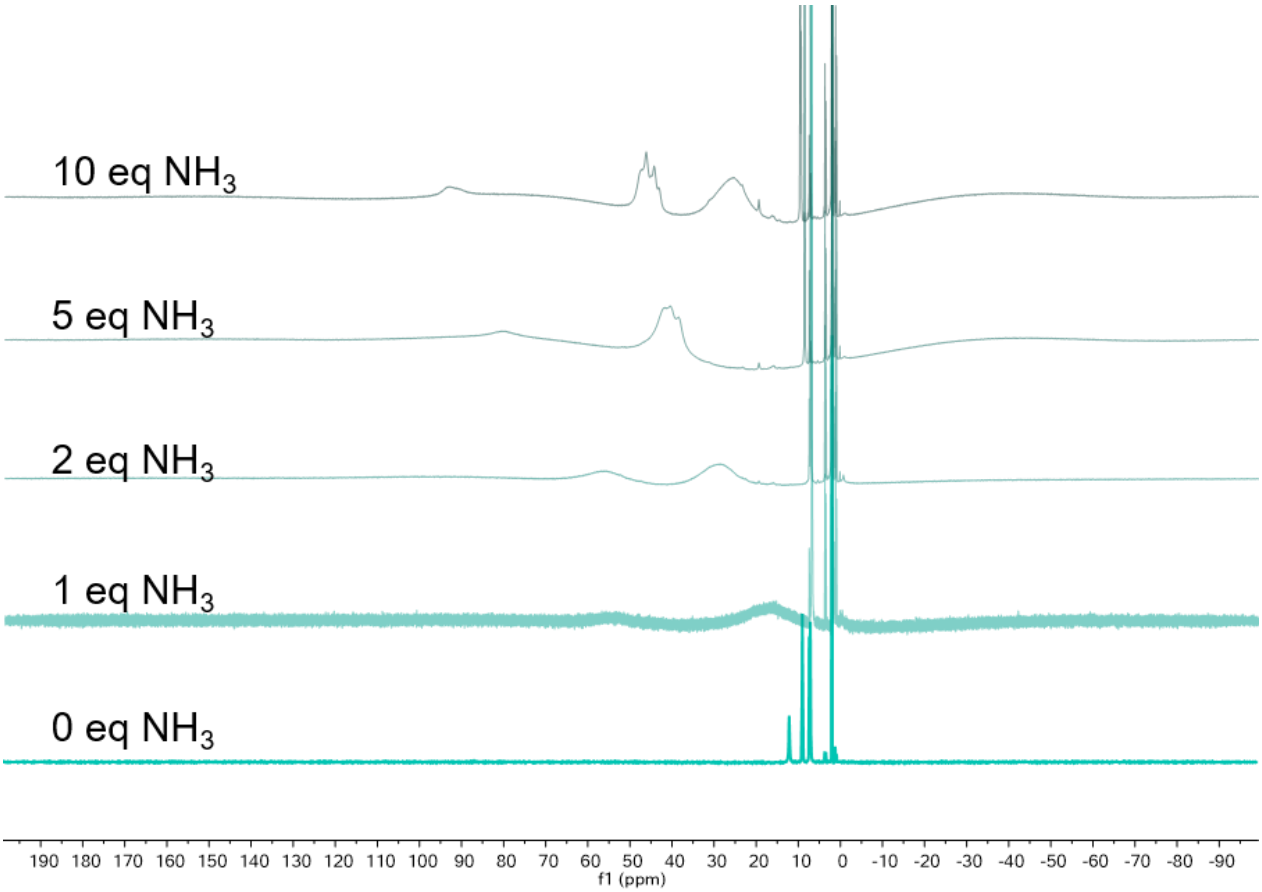

Figure S32: ^{1}H NMR (400 MHz) spectrum of [(TPA)Fe(MeCN)$_2$]OTf$_2$ in CD_3CN with 0, 1, 2, 5, and 10 equivalents of NH_3 added via calibrated bulb to a J. Young NMR tube.

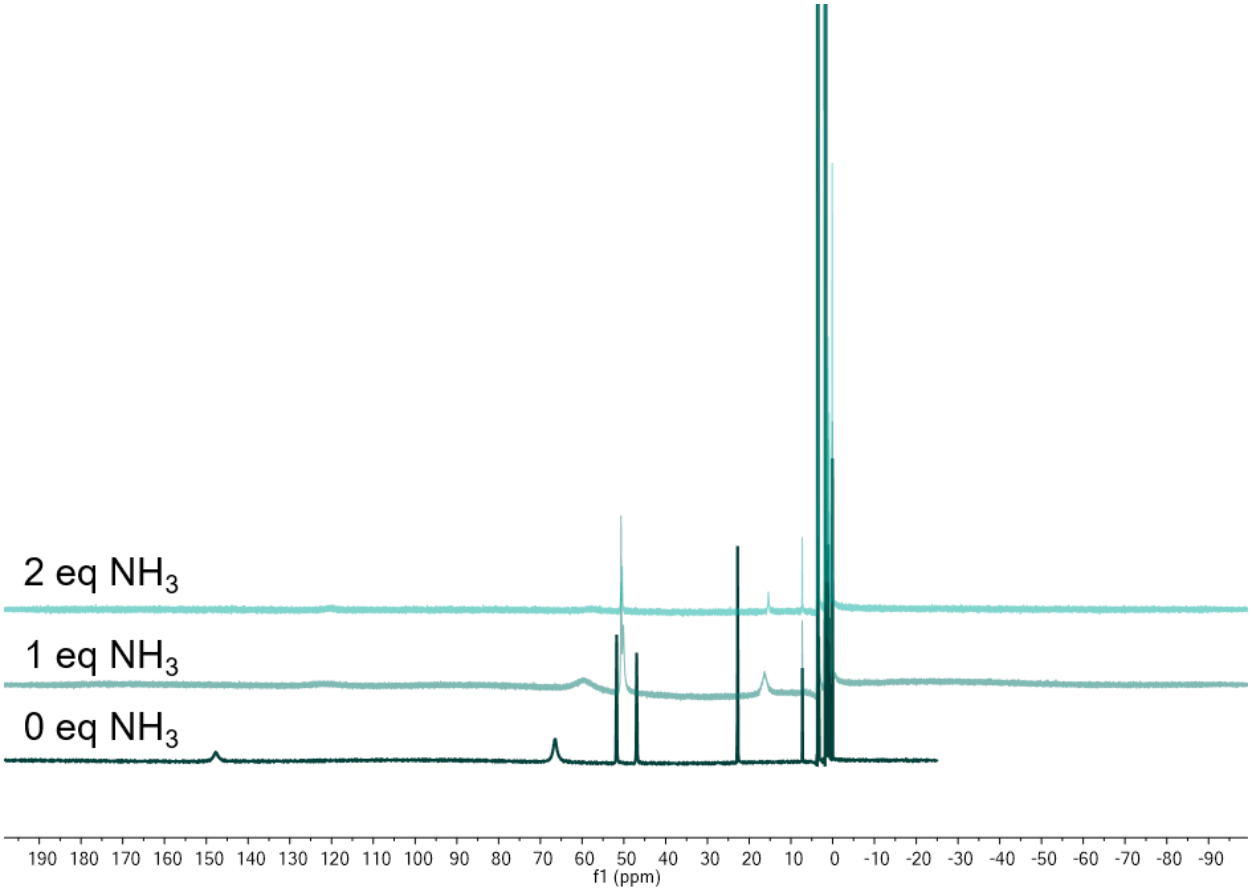

Figure S33: ^{1}H NMR (400 MHz) spectrum of (TPA)Fe(OTf)$_2$ in d8-THF with 0, 1, and 2 equivalents of NH_3 added via calibrated bulb to a J. Young NMR tube. The loss in intensity upon addition of ammonia is due to precipitation.

S13. Mössbauer spectroscopy of $[(TPA)Fe(L)_2]^{2+}$ species

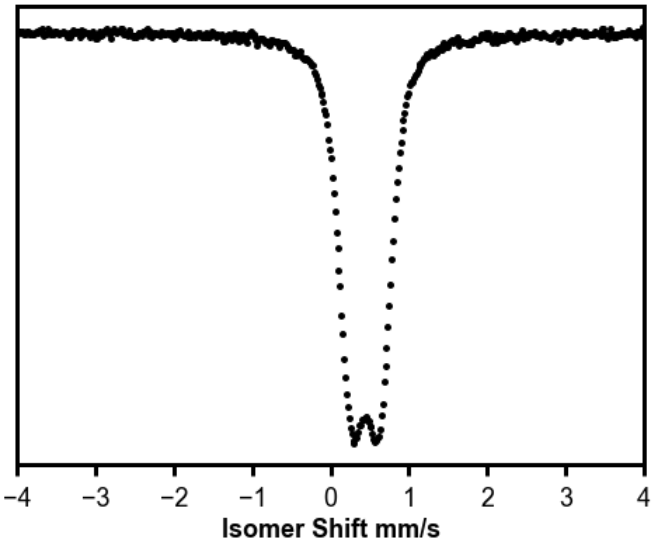

Figure S34: Mössbauer spectrum of $[(TPA)Fe(MeCN)_2]OTf_2$ recorded at 80 K. The isomer shift δ (mm/s) is 0.44, and the absolute value of the quadrupole splitting |ΔEQ| (mm/s) is 0.34.

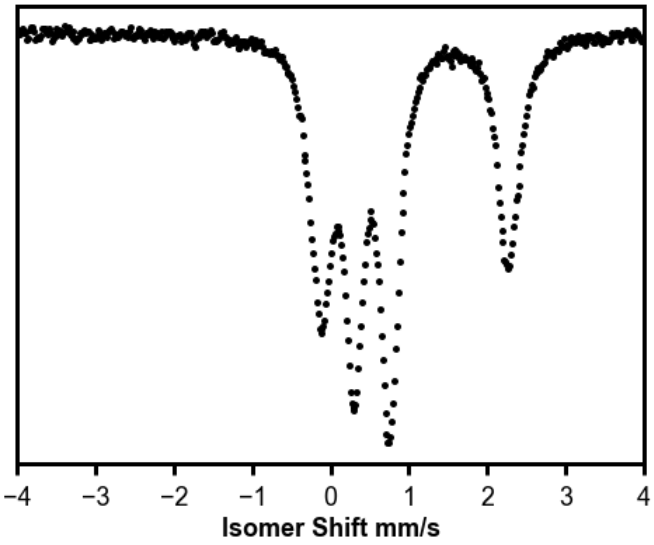

Figure S35: Mössbauer spectrum of crystalline $[(TPA)Fe(NH_3)_2]OTf_2$ recorded at 100 K.

The Mössbauer spectrum at 100 K, the temperature that diffraction data was collected at, can be fit by two quadrupole doublets. One doublet has isomer shift 1.06 mm/s and quadrupole splitting 2.38 mm/s, and the second has isomer shift 0.52 mm/s and quadrupole splitting 0.47 mm/s. Asymmetry in the quadrupole doublets is observed; this is likely due to the anisotropic orientation of the needle-like crystalline sample in the Mössbauer cup. The relative peak areas of these quadrupole doublets are 0.45:0.55, respectively. These quadrupole doublets are in agreement with the presence of both high spin and low spin Fe(II) in similar abundance; this is in agreement with the observed ratio of high spin and low spin Fe(II) in the solid state structure.

S14. ATR-IR spectrum of $[(TPA)Fe(NH_3)_2]OTf_2$

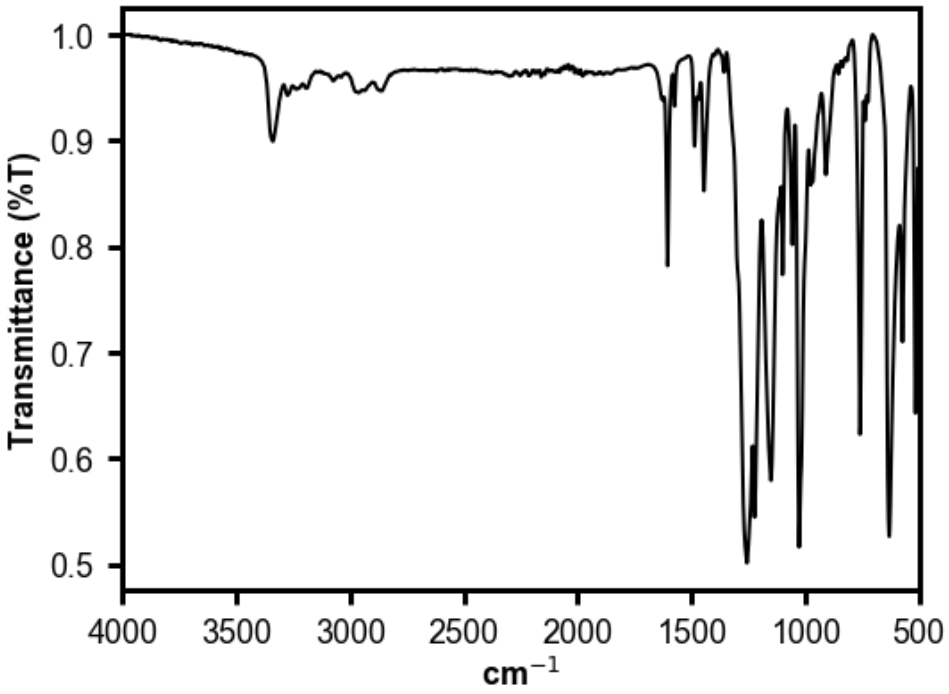

Figure S36: ATR-IR spectrum of a solid sample of crystalline $[(TPA)Fe(NH_3)_2]OTf_2$.

S15. UV-Vis spectrum of $[Fe(NH_3)_6]OTf_2$

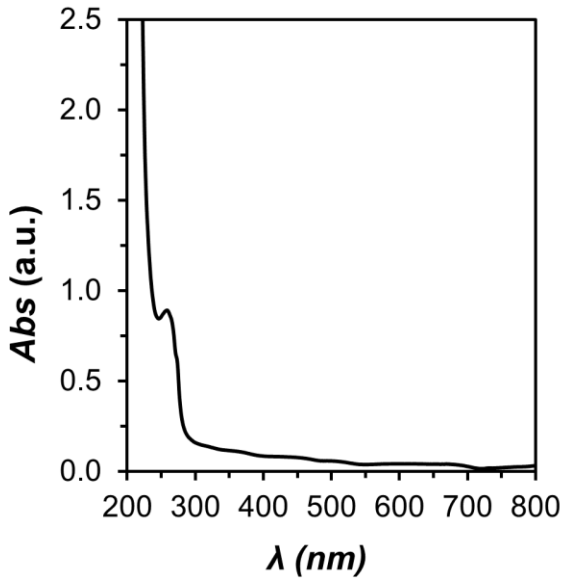

Figure S37: UV-Vis spectrum of 0.4 mM $[Fe(NH_3)_6]OTf_2$ formed by dissolving $FeOTf_2$ in a 2 M NH_3 solution.

S16. Electrochemistry of the first redox process (E_1)

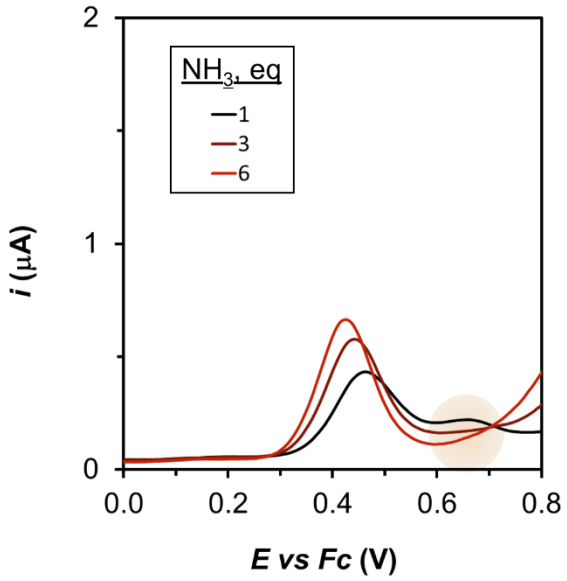

Figure S38: Differential pulse voltammograms in acetonitrile with 0.5 mM [(TPA)Fe(MeCN)$_2$]OTf$_2$ and 0.05 M NH_4OTf at low ammonia concentrations reflecting the equilibrium character in the substitution of MeCN by NH_3 in the coordination sphere of $[(TPA)Fe]^{2+}$, since the feature at 0.65 V corresponds to remaining $[(TPA)Fe(MeCN)_2]^{2+}$.

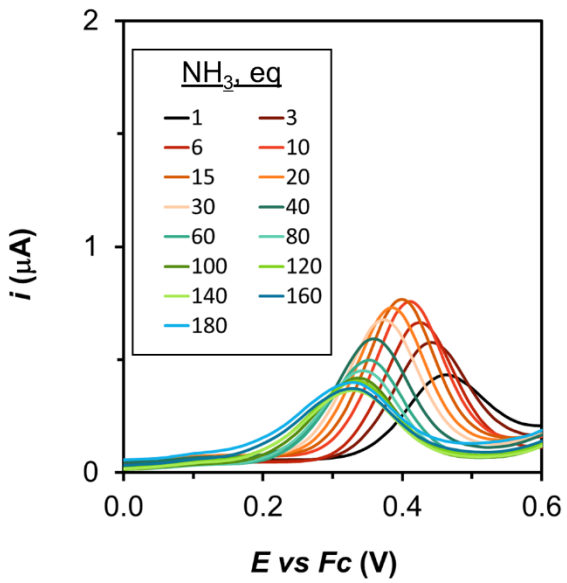

Figure S39: Differential pulse voltammograms in acetonitrile with 0.5 mM [(TPA)Fe(MeCN)$_2$]OTf$_2$ and 0.05 M NH_4OTf with varying ammonia concentrations.

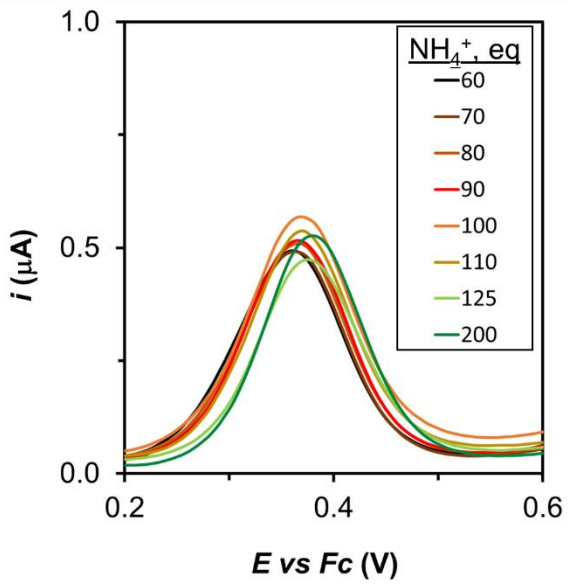

Figure S40: Differential pulse voltammograms in acetonitrile with 0.5 mM $[(TPA)Fe(MeCN)_2]OTf_2$, 0.025 M NH_3, and varying NH_4OTf concentration.

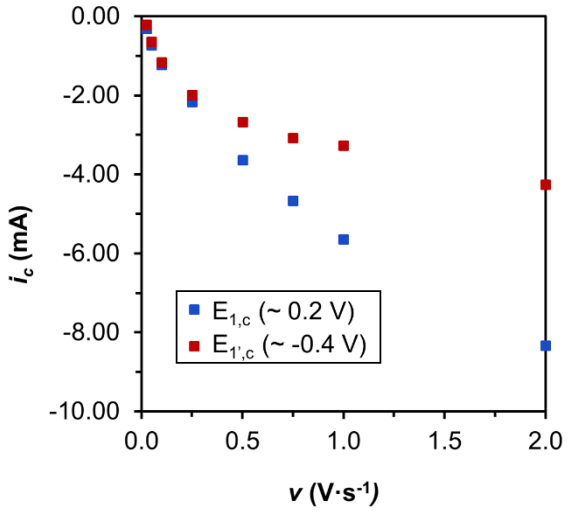

Figure S41: Intensity of the cathodic peaks at the potential $E_{1,c}$ and $E_{1',c}$ depending on the scan rate. At low scan rates, both peaks show similar intensities corresponding to similar concentrations of species $[(TPA)Fe^{III}(NH_3)_2]^{3+}$ and $[(TPA)Fe^{III}(NH_3)(NH_2)]^{2+}$. As the scan rate increases, the intensity of the $[(TPA)Fe^{III}(NH_3)_2]^{3+}$ reductive peak at around 0.2 V decreases faster than the one corresponding to $[(TPA)Fe^{III}(NH_3)(NH_2)]^{2+}$, indicating higher concentrations of the former due to the scan rate being faster than the deprotonation equilibrium. Both intensity values were measured with respect to the anodic baseline due to difficulties in establishing the baseline from the cathodic scan arising from the proximity of both redox events E_1 and E_2.

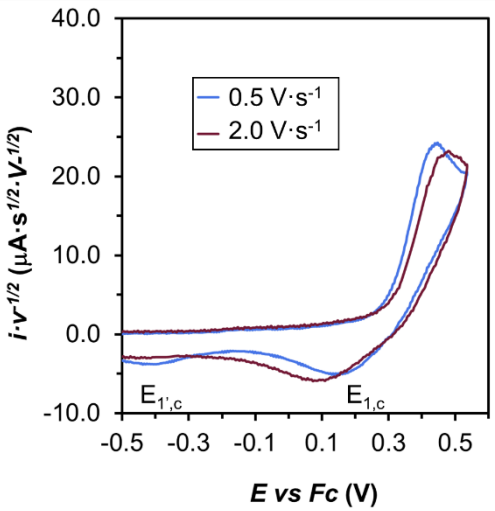

Figure S42: CV of an acetonitrile solution containing 0.5 mM (TPA)Fe(MeCN)$_2$]OTf$_2$, 0.05 M NH_4OTf, and 0.05 M NH_3 performed at two scan rates to show the different ratio of the intensities at $E_{1,c}$ and $E_{1',c}$.

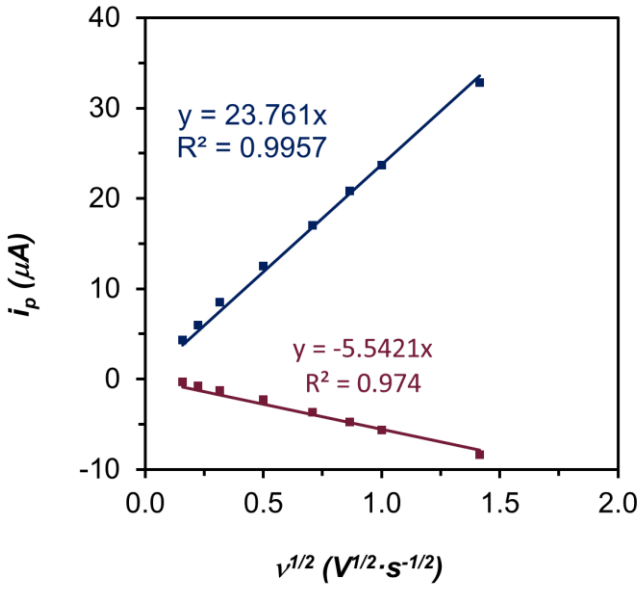

Figure S43: Plot of the intensity of the anodic (blue) and cathodic (red) scans in the precatalytic wave centered at E_1 versus the square root of the scan rate according to the Randles-Sevcik equation. Both intensity values were measured with respect to the anodic baseline due to difficulties in establishing the baseline from the cathodic scan arising from the proximity of both redox events E_1 and E_2. This fact, together with the equilibrium between $[(TPA)Fe^{III}(NH_3)_2]^{3+}$ and $[(TPA)Fe^{III}(NH_3)(NH_2)]^{2+}$, accounts for the difference in the cathodic and anodic intensities.

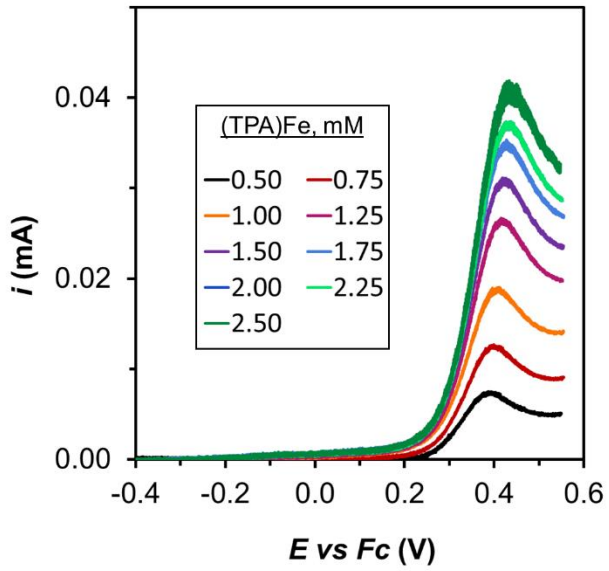

Figure S44: Linear sweep voltammograms recorded at 100 $mV \cdot s^{-1}$ in a MeCN solution containing, 0.05 M NH_3, 0.05 M NH_4OTf, and different concentrations of $[(TPA)Fe(MeCN)_2]OTf_2$.

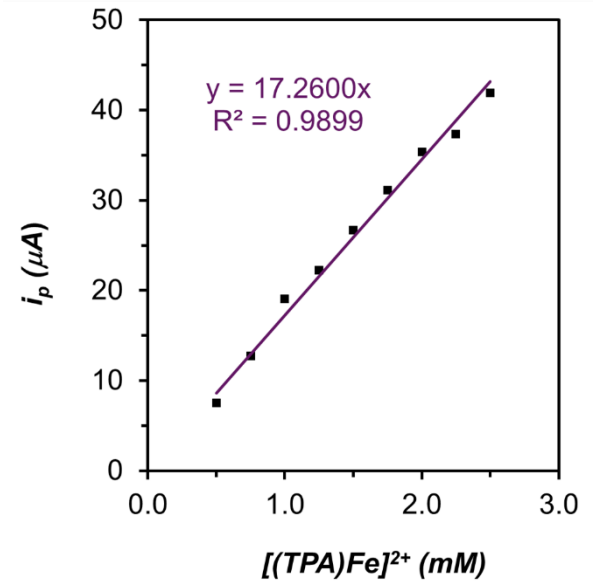

Figure S45: Plot of the intensity of the precatalytic wave E_1 at different $[(TPA)Fe(MeCN)_2]OTf_2$ concentrations.

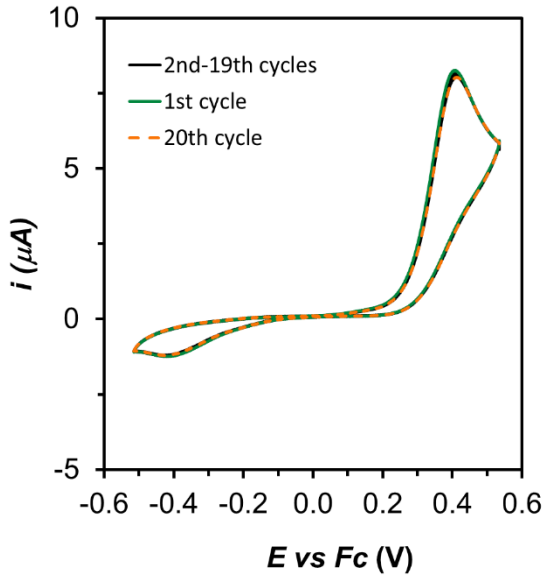

Figure S46: Successive cyclic voltammograms in an acetonitrile solution containing 0.5 mM $[(TPA)Fe(MeCN)_2]OTf_2$, 0.05 M NH_3, and 0.05 M NH_4OTf, showing the high stability of the first redox event.

S17. Electrochemistry of the catalytic process (E_2) based on Nernstian behavior

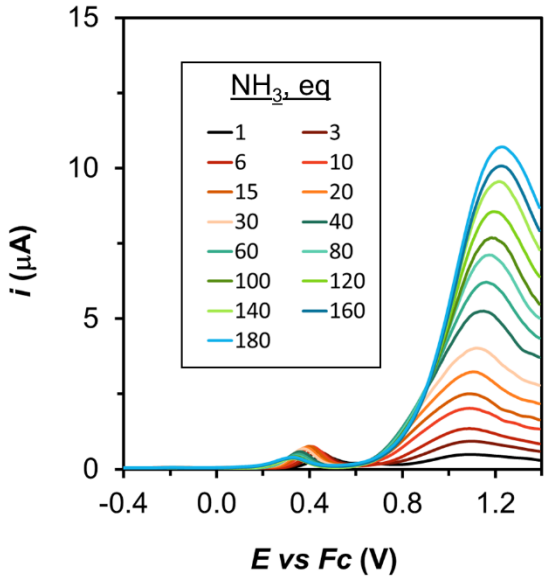

Figure S47: Differential pulse voltammograms in acetonitrile of 0.5 mM $[(TPA)Fe(MeCN)_2]OTf_2$, 0.05 M NH_4OTf, and varying ammonia concentrations.

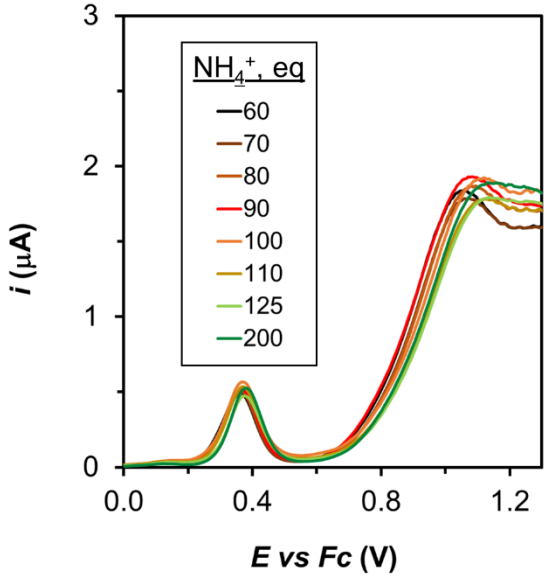

Figure S48: Differential pulse voltammograms in acetonitrile of 0.5 mM $[(TPA)Fe(MeCN)_2]OTf_2$, 0.025 M NH_3, and varying NH_4OTf concentration.

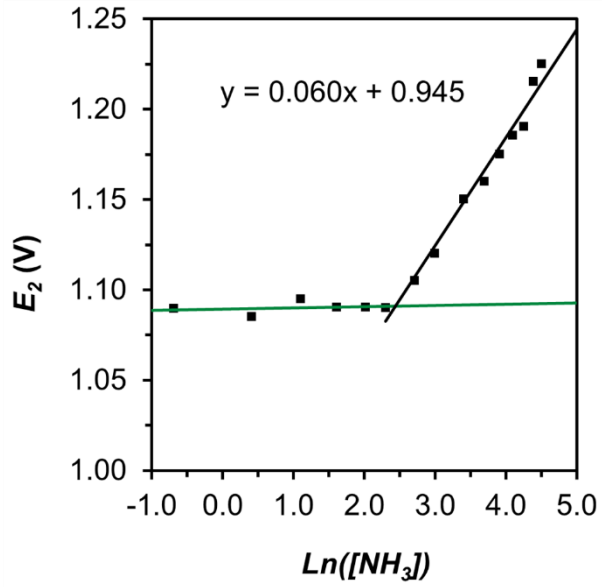

Figure S49: Plot of the potential for the first redox event E_2 versus the natural logarithm of the ammonia concentration. E_2 values were estimated from DPV experiments. At low ammonia concentrations the constant value of E_2 is consistent with an EC_{cat} mechanism.[7] The increase in E_2 at higher concentrations of ammonia suggests a non-Nernstian behavior arising from a chemical step faster than electron transfer.[8]

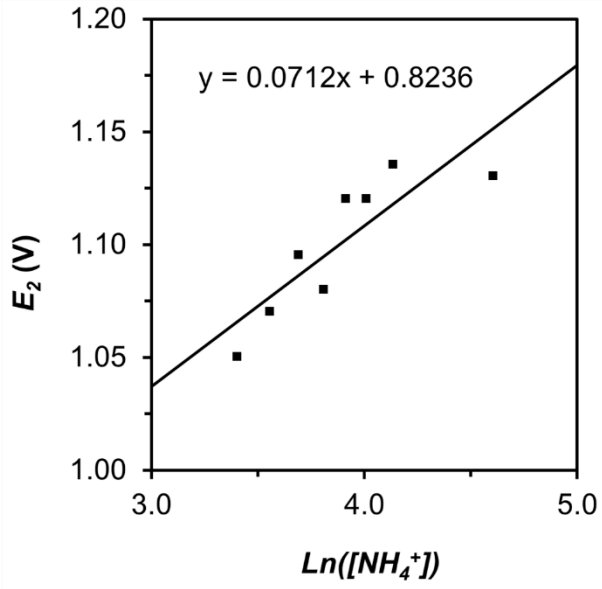

Figure S50: Plot of the potential for the first redox event E_2 versus the natural logarithm of the NH_4OTf concentration. E_2 values were estimated from DPV experiments. The increase in E_2 at higher concentrations of ammonia suggests a non-Nernstian behavior arising from a chemical step faster than electron transfer.

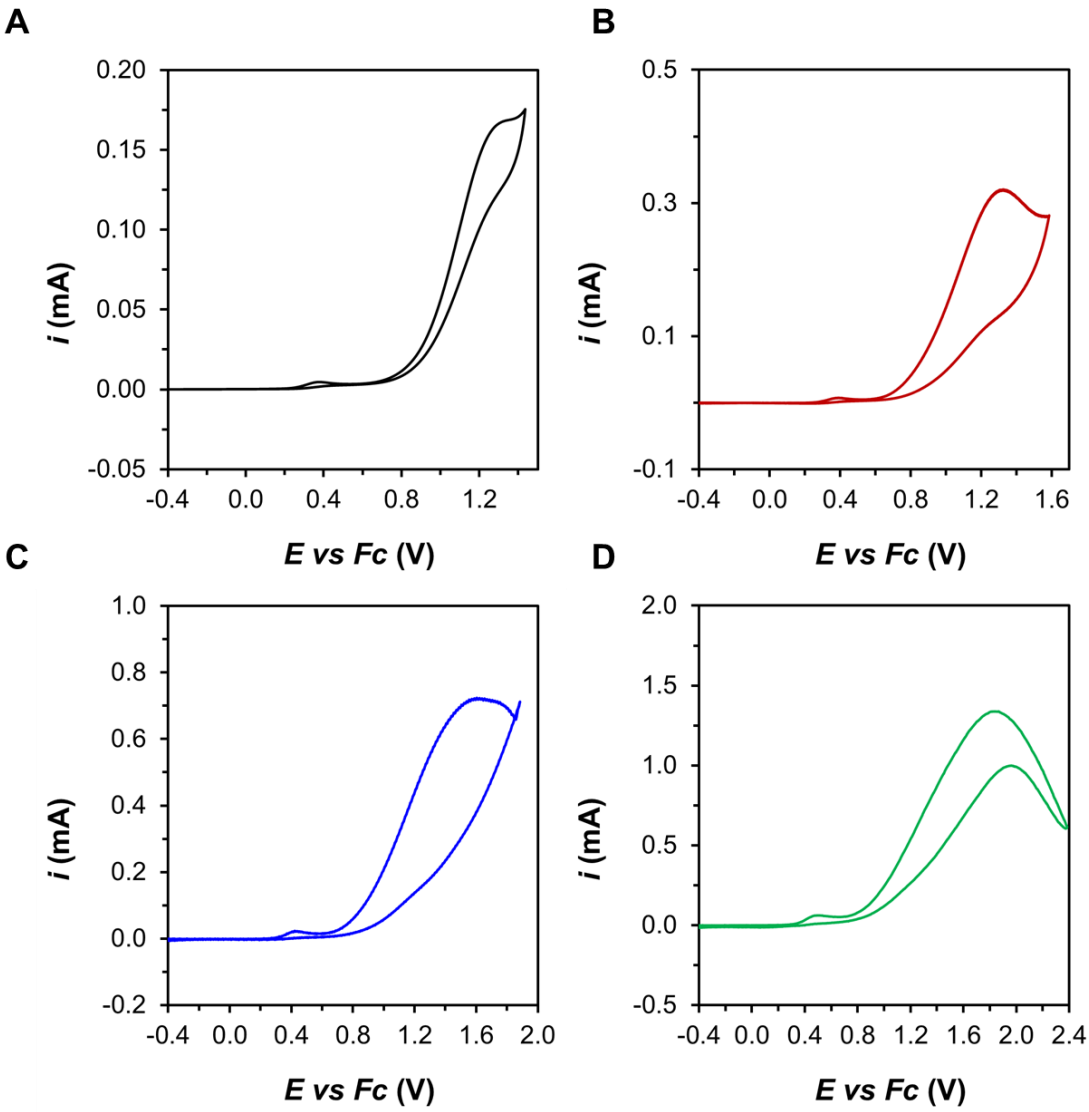

Figure S51: Background corrected CV recorded at (A) 0.01 $V \cdot s^{-1}$, (B) 0.1 $V \cdot s^{-1}$, (C) 1 $V \cdot s^{-1}$, and (D) 10 $V \cdot s^{-1}$ in a MeCN solution containing 0.5 mM $[(TPA)Fe(MeCN)_2]OTf_2$, 0.05 M NH_3, and 0.05 M NH_4OTf. Results show the deviation from ideal S-shape response in the whole range of studied scan rates.

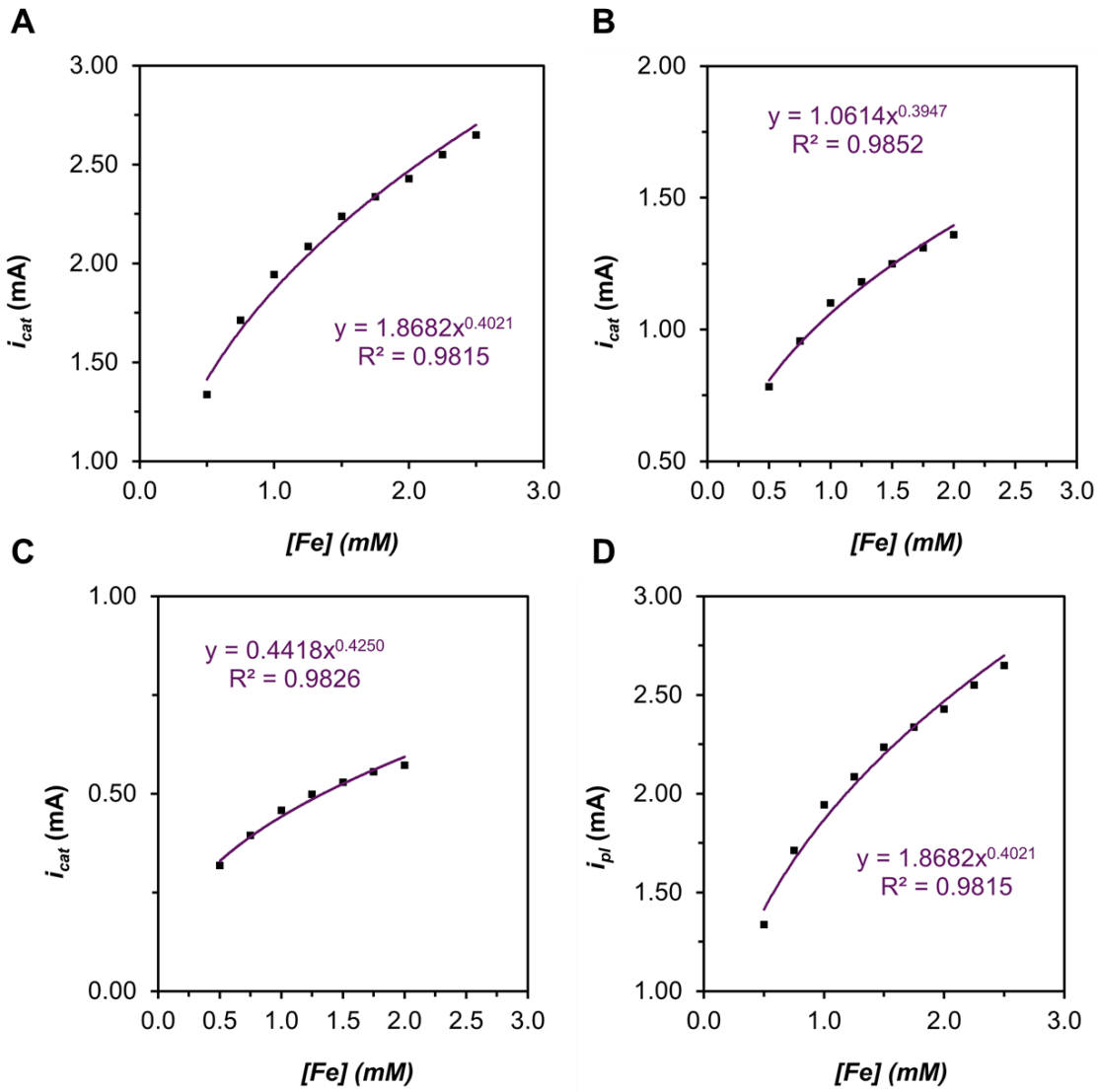

Figure S52: Plot of the intensity of the catalytic wave (i_{cat}) in CVs obtained at (A) 10 $V \cdot s^{-1}$, (B) 1 $V \cdot s^{-1}$, (C) 0.1 $V \cdot s^{-1}$, and (D) 0.01 $V \cdot s^{-1}$ at different $[(TPA)Fe(MeCN)_2]OTf_2$ concentrations. In all cases, the apparent order of reaction in $[(TPA)Fe(MeCN)_2]OTf_2$ is lower than 1 and does not seem to change with the scan rate. This behavior is consistent with the electron transfer to the electrode being the rate determining step of the catalytic process resulting in non-Nernstian behavior.

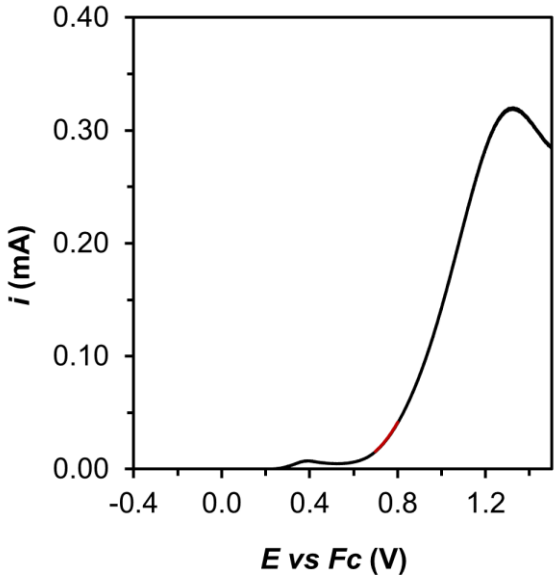

Figure S53: Background corrected linear sweep voltammetry (LSV) recorded at 100 $mV \cdot s^{-1}$ in a MeCN solution containing 0.5 mM $[(TPA)Fe(MeCN)_2]OTf_2$, 0.05 M NH_3, and 0.05 M NH_4OTf. Red trace shows the data range employed for performing the FOWA.

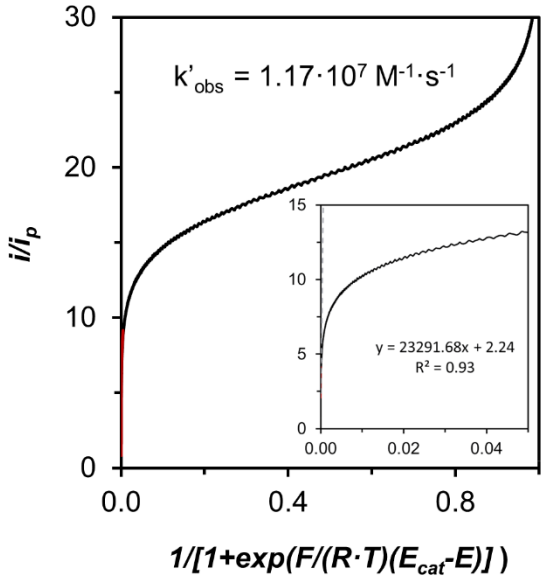

Figure S54: FOWA for a EC_{cat} mechanism[9] calculated from the previous linear sweep voltammetry (Figure S53) recorded at 100 $mV \cdot s^{-1}$ in a MeCN solution containing 0.5 mM $[(TPA)Fe(MeCN)_2]OTf_2$, 0.05 M NH_3, and 0.05 M NH_4OTf. The convex form obtained in the curve is consistent with a non-Nernstian behavior as previously reported.[8] E_{cat} was determined as the potential for the half-wave catalytic current.

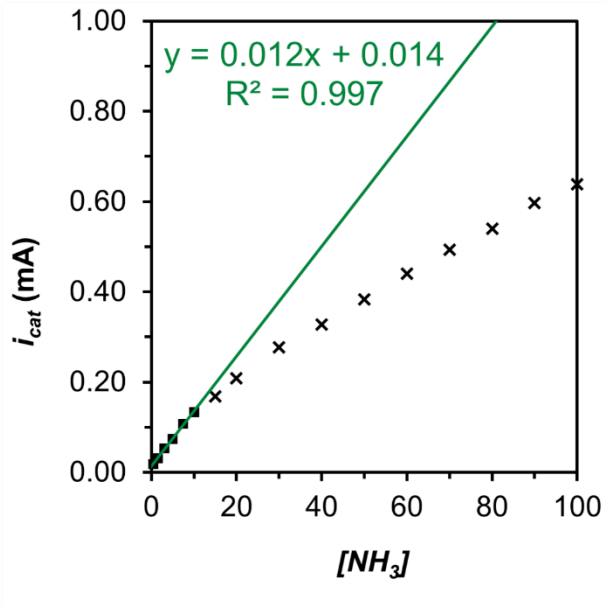

Figure S55: Plot of the intensity of the catalytic wave (i_{cat}) from CV obtained at 100 $mV \cdot s^{-1}$ at different NH_3 concentrations using 0.5 mM $[(TPA)Fe(MeCN)_2]OTf_2$ and 0.05 M NH_4OTf. For the low ammonia concentration, the catalytic current follows a linear trend suggesting first order in NH_3. At higher ammonia concentration, the fast catalysis obtained deviates from Nernstian behavior as previously evidenced and the apparent order of reaction is lower than 1.

S18. Discussion of the non-Nernstian behavior in catalytic process (E_2)

The equations governing the electrochemical behavior of an EC_{cat} mechanism depend again on the regime of the voltammetry response in the kinetic zone diagram for catalytic processes. The easiest mathematical treatment is obtained with the S-shape response when the intensity of the catalytic wave purely depends on the kinetics of the process rather than the diffusion of substrate to the electrode.[7] Unfortunately, no pure S-shape has been found in the whole range of analyzed scan rates as previously shown. In fact, analysis of the dependence of the catalytic current i_{cat} on the catalyst concentration revealed a non-linear relationship with an apparent order of reaction close to 0.5 for all of the different scan rate values. This is in contrast with the linear response expected for a pseudo-first order reaction according to the following equation:

$$i_{pl} = 6FSC^0_{cat}\sqrt{D_{cat}}\sqrt{k_e C^0_{NH_3}} \quad (1)$$

Influence of a fast deactivation process as responsible for the apparent order of reaction lower than 1 can be ruled out in the CV time scale based on the reproducibility of the CV upon 50 cycles. The deactivation process found during CPC experiments leading to Fe deposition on the electrode operates at a much longer timescale so that it is unlikely to affect the order of reaction obtained by CV. Moreover, in the EC_{cat} mechanism, the potential for the half wave of the catalytic process ($E_{cat/2}$) should be constant and independent of the concentration of substrate (NH_3). However, we have found a linear dependence between the $E_{cat/2}$ and the ln[NH_3], which features a positive slope of 0.06. Only at very low concentrations of NH_3, the potential is constant as expected. Proper treatment of the obtained diffusion controlled waves by the foot of the wave analysis (FOWA) leads to a convex curvature in the FOWA plot which, together with the observed increase in the $E_{cat/2}$ with increasing [NH_3], is typical from a non-Nernstian behavior in the electron transfer step.[8] In such cases, other theories such as the Butler-Volmer law or Marcus-Husch model have to be applied to model the electron transfer between the catalyst and the electrode.[10] This fact might be explained by a catalytic process with a large kinetic rate so that the kinetic of the electron transfer starts to have an influence in the overall response. The influence of the electron transfer rate might also account for the apparent 0.5 order of reaction, as only a fraction of the catalyst is oxidized to the active species. In such cases, equations have been derived using the Butler-Volmer law that includes the charge transfer coefficient (α) and the rate constant for interfacial electron transfer (k_s).

S19. Electrochemistry of the catalytic process (E_2) based on Butler-Volmer law

Determination of α, k_s and D_{cat} can be achieved based on the following equations describing the CV response of an electron transfer following the Butler-Volmer law:

$$i_p = 0.496FSC^0_{cat}\sqrt{D_{cat}}\sqrt{\frac{\alpha F v}{RT}} \qquad (2)$$

$$E_{p,c} = E^0 + 0.78\frac{RT}{\alpha F} - \frac{RT}{\alpha F}\ln\left(k_s\sqrt{\frac{RT}{\alpha F v D_{cat}}}\right) \qquad (3)$$

Due to the extremely fast catalytic character of the wave at E_2 and the impossibility of obtaining reversible behavior at that potential, we have used the precatalytic wave E_1 as a reference to obtain those values as the species involved in both processes are expected to have similar properties.

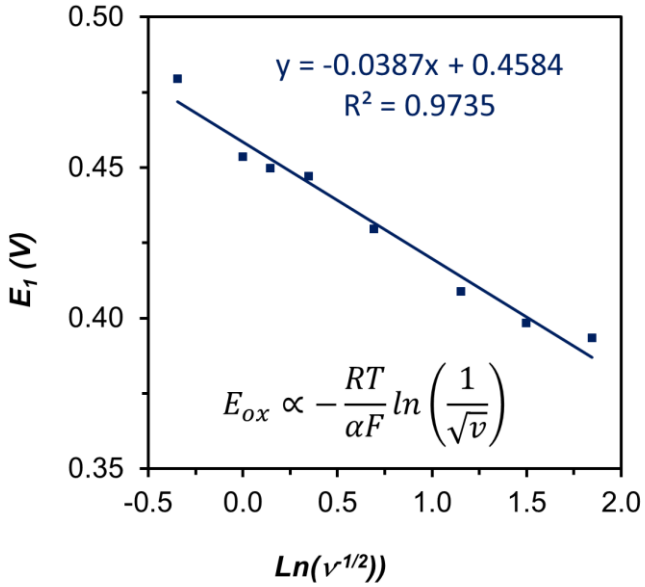

Figure S56: Plot of the E_1 potential of the anodic peak in the precatalytic wave versus $\mathrm{Ln}(1/v^{-1/2})$ following the equation for the potential using the Butler-Volmer law. The slope of that plot allows a value of 0.66 for α to be obtained.

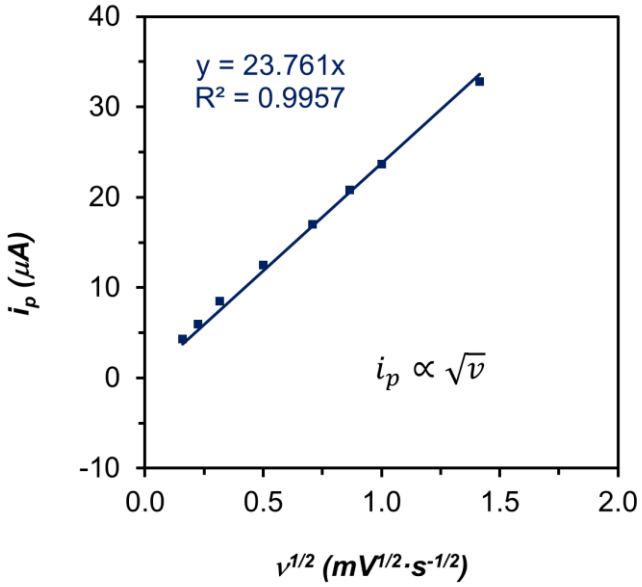

Figure S57: Plot of the intensity of the anodic scans in the precatalytic wave centered at E_1 versus the square root of the scan rate.

D_{cat} has been determined from the slope in previous plot of the intensity of the peak at E_1 versus the square root of the scan rate, resulting in a value of $9.5 \cdot 10^{-10}$ $m^2 \cdot s^{-1}$. Then, using α, D_{cat} and the equation for the previous anodic peak potential with an E^0 of 0.3 V determined from $E_{1/2} = (E_{1,a}+E_{1,c})/2$, the calculated value of k_s is 111 $m \cdot s^{-1}$.

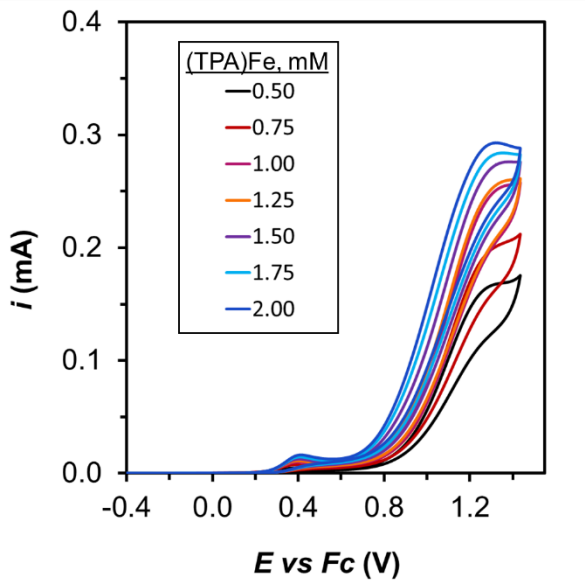

Figure S58: Cyclic voltammograms recorded at 10 $mV \cdot s^{-1}$ in a MeCN solution containing, 0.05 M NH_3, 0.05 M NH_4OTf, and different concentrations of $[(TPA)Fe(MeCN)_2]OTf_2$.

Procedure for the Foot-of-the-wave analysis performed in each condition:

Foot of the wave analysis was performed by using the equations deducted for EC_{cat} obeying the Butler –Volmer law[11], following the next equation:

$$FIT\left(E^0_{P/Q} - E\right) = \frac{\frac{i}{i_p}}{1 - 0.446\frac{i}{i_p}\frac{\sqrt{D_{cat}}}{k_s}\sqrt{\frac{F}{R\cdot T}v}\exp\left[\alpha\frac{F}{R\cdot T}\left(E^0_{cat} - E\right)\right]} = \frac{n\cdot 2.24\cdot\sqrt{\frac{R\cdot T}{F\cdot v}\cdot k'_{obs}}}{1+\exp\left[\frac{F}{R\cdot T}\left(E^0_{cat} - E\right)\right]} \qquad (4)$$

F is the Faraday constant, R is the gas constant, T is the temperature. The parameters α, k_s and D_{cat} have been previously obtained using the precatalytic wave as model for the electron transfer. In this case, n = 6 due to the 6 electrons involved in the catalytic ammonia oxidation to molecular nitrogen. The intensity of the one-electron wave (i_p) has been estimated from the one-electron oxidation precatalytic wave at *E1* for each condition. E^0_{cat} has been determined as the potential of the half-wave for the catalytic process. For each condition, involving concentration of catalyst, concentration of NH_3 and scan rate (*v*), the FOWA has been performed in similar regions of the potential range in order to allow a fair comparison upon changing the conditions. This region has been selected as the foot of the wave region where the plot of FIT versus $1/(1+\exp[F/(RT)(E_{cat}-E)])$ behaves linearly ($R^2 > 0.85$). Then, from the slope of that plot, the apparent pseudo-first order rate constant k'_{obs} can be obtained and thus the value of the apparent second-order rate constant k_{obs}. A representative example of this methodology is shown below for one specific condition.

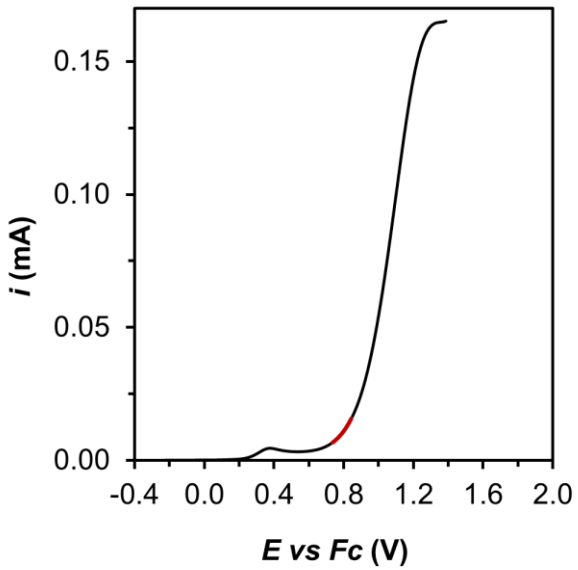

Figure S59: Background corrected linear sweep voltammetry (LSV) recorded at 10 $mV\cdot s^{-1}$ in a MeCN solution containing 0.5 mM $[(TPA)Fe(MeCN)_2]OTf_2$, 0.05 M NH_3, and 0.05 M NH_4OTf. Red trace shows the data range employed for performing the FOWA.

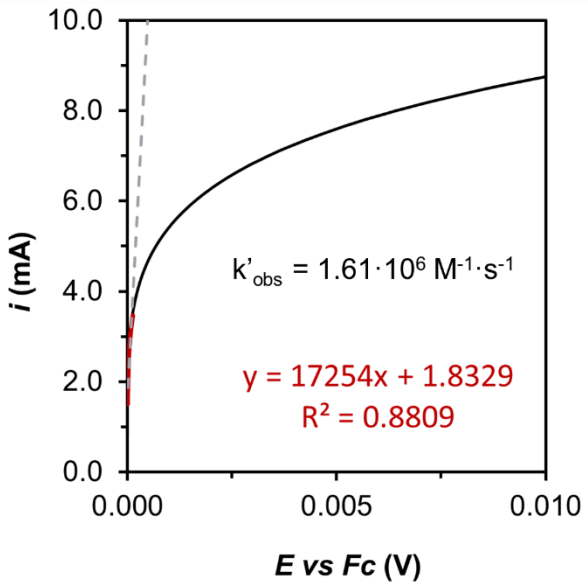

Figure S60: FOWA for an EC_{cat} mechanism obeying the Butler–Volmer law calculated from previous linear sweep voltammetry recorded at 10 $mV \cdot s^{-1}$ in a MeCN solution containing 0.5 mM $[(TPA)Fe(MeCN)_2]OTf_2$, 0.05 M NH_3, and 0.05 M NH_4OTf.

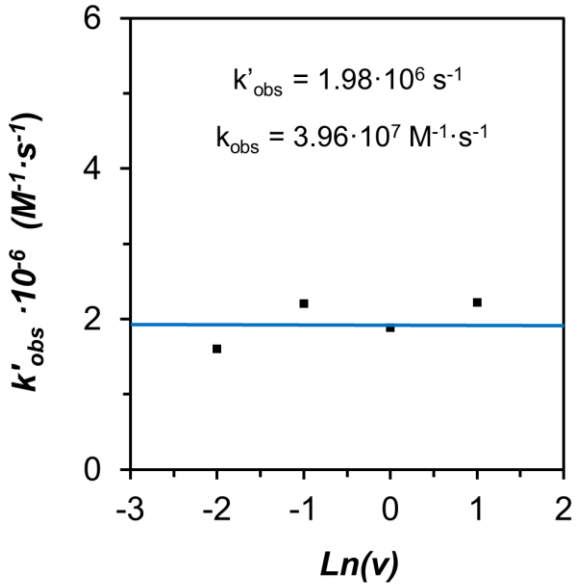

Figure S61: Plot of the k'_{obs} calculated by FOWA from LSV using 0.5 mM $[(TPA)Fe(MeCN)_2]OTf_2$, 0.05 M NH_3, and 0.05 M NH_4OTf at different scan rates versus the natural logarithm of the scan rate. The observed independence leading to an average value of $1.98 \cdot 10^6$ s^{-1} is consistent with the assumed mechanism.

S20. Reversible binding of TPA to $FeOTf_2$

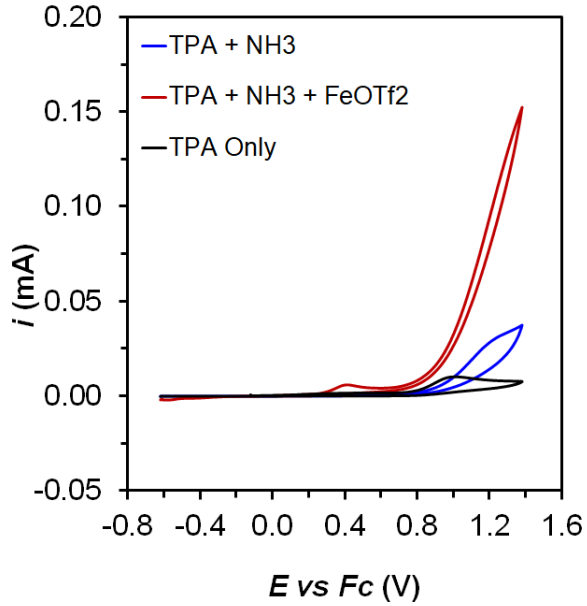

Figure S62: Cyclic voltammograms in acetonitrile with 50 mM NH_4OTf and (black) free TPA, (red) free TPA and 65 mM NH_3, and (blue) free TPA, 65 mM NH_3, and 0.5 mM $FeOTf_2$ added sequentially to demonstrate the ability of $FeOTf_2$ to rebind TPA after demetallation.

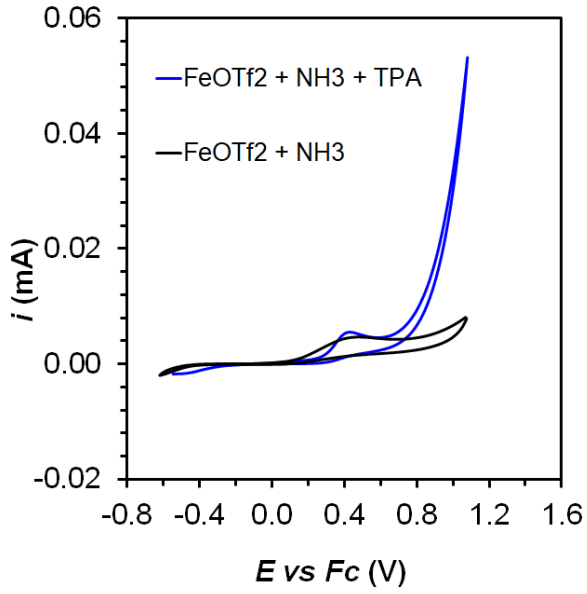

Figure S63: Cyclic voltammograms in acetonitrile with 0.5 mM $FeOTf_2$, 50 mM NH_3, and 50 mM NH_4OTf in the absence of added TPA (black) and in the presence of TPA (blue). Free TPA was added to the iron(II) triflate solution to show that it can rebind after demetallation and coordination of ammonia.

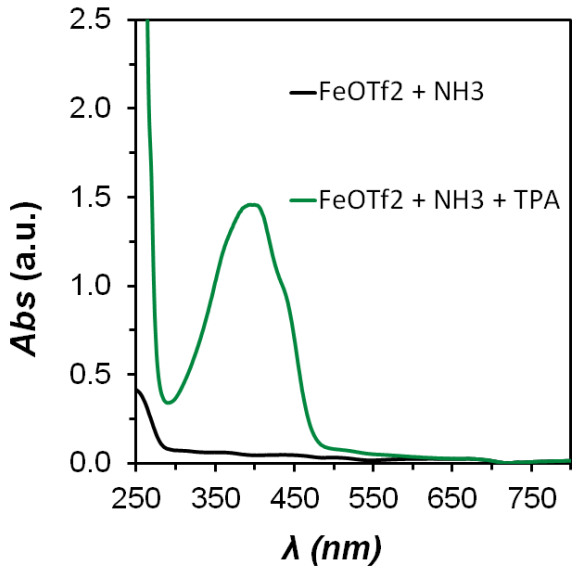

Figure S64: UV-Vis spectra in acetonitrile with 0.5 mM $FeOTf_2$, 50 mM NH_3, and 50 mM NH_4OTf in the absence of added TPA (black) and in the presence of TPA (blue). Free TPA was added to the iron(II) triflate solution to show that it can rebind after demetallation and coordination of ammonia.

S21. Electrochemistry of (TPA)Fe in presence of hydrazine

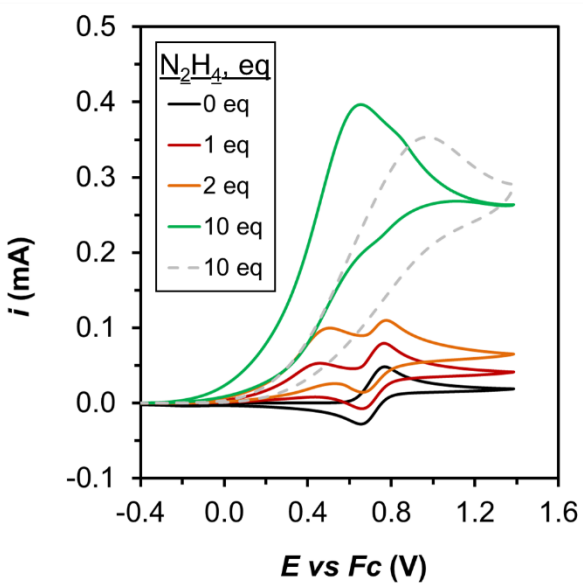

Figure S65. CV experiments of an acetonitrile solution containing 2.5 mM of $[(TPA)Fe(MeCN)_2]^{2+}$ with increasing concentrations of N_2H_4. The grey dashed line shows the background current using 10 equivalents of hydrazine in the absence of (TPA)Fe complex. BDD was used as the working electrode, and the scan rate was set to 100 $mV \cdot s^{-1}$.

S22. References

[1] Canary, J. W.; Wang, Y.; Roy, R. Tris[(2-pyridyl)methyl]amine (TPA) and (+)-bis[(2-pyridyl)methyl]-1-(2-pyridyl)-ethylamine (α-METPA). *Inorg. Synth.* **1998**, *32*, 70-75.

[2] Diebold, A.; Hagen, K. S. Iron(II) Polyamine Chemistry: Variation of Spin State and Coordination Number in Solid State and Solution with Iron(II) Tris(2-pyridylmethyl)amine Complexes. *Inorg. Chem.* **1998**, *37*, 215-223.

[3] Sheldrick, G. SHELXT - Integrated Space-Group and Crystal-Structure Determination. *Acta Crystallogr., Sect. C: Struct.* **2015**, *71*, 3-8.

[4] Dolomanov, O. V.; Bourhis, L. J.; Gildea, R. J.; Howard, J. A. K.; Puschmann, H. OLEX2: a Complete Structure Solution, Refinement and Analysis Program. *J. Appl. Crystallogr.* **2009**, *42*, 339-341.

[5] Macpherson, J. V. A Practical Guide to Using Boron Doped Diamond in Electrochemical Research. *Phys. Chem. Chem. Phys.* **2015**, *17*, 2935-2949.

[6] Lindley, B. M.; Appel, A. M.; Krogh-Jespersen, K.; Mayer, J. M.; Miller, A. J. M. Evaluating the Thermodynamics of Electrocatalytic N_2 Reduction in Acetonitrile. *ACS Energy Lett.* **2016,** *1*, 698-704.

[7]Costentin, C.; Savéant, J. M. Elements of Molecular and Biomolecular Electrochemistry: An Electrochemical Approach to Electron Transfer Chemistry, John Wiley & Sons, Hoboken, 2006.

[8] Wang, V. C.-C.; Johnson, B. A. Interpreting the Electrocatalytic Voltammetry of Homogeneous Catalysts by the Foot of the Wave Analysis and Its Wider Implications. *ACS Catal.* **2019**, *9*, 7109-7123.

[9] Costentin, C.; Drouet, S.; Robert, M.; Savéant, J.-M. Turnover Numbers, Turnover Frequencies, and Overpotential in Molecular Catalysis of Electrochemical Reactions. Cyclic Voltammetry and Preparative-Scale Electrolysis. *J. Am. Chem. Soc.* **2012**, *134*, 11235-11242.

[10] Costentin, C.; Robert, M.; Savéant, J.-M. Catalysis of the Electrochemical Reduction of Carbon Dioxide. *Chem. Soc. Rev.* **2013**, *42*, 2423-2436.

[11] Costentin, C.; Drouet, S.; Robert, M.; Savéant, J.-M. A Local Proton Source Enhances CO_2 Electroreduction to CO by a Molecular Fe Catalyst. *Science* **2012**, *338*, 90-94.